

# Nanoscale Core–Shell Hyperbolic Structures for Ultralow Threshold Laser Action: An Efficient Platform for the Enhancement of Optical Manipulation

Hung-I Lin,<sup>†,‡,○</sup> Kanchan Yadav,<sup>§,⊥,○</sup> Kun-Ching Shen,<sup>#</sup> Golam Haider,<sup>‡,○</sup> Pradip Kumar Roy,<sup>‡</sup> Monika Kataria,<sup>‡,○</sup> Ting-Jia Chang,<sup>‡</sup> Yao-Hsuan Li,<sup>†</sup> Tai-Yuan Lin,<sup>∇</sup> Yit-Tsong Chen,<sup>§,○</sup> and Yang-Fang Chen<sup>\*,†,‡,||</sup>

<sup>†</sup>Graduate Institute of Applied Physics, <sup>‡</sup>Department of Physics, <sup>§</sup>Department of Chemistry, and <sup>||</sup>Advanced Research Center for Green Materials Science and Technology, National Taiwan University, Taipei 106, Taiwan

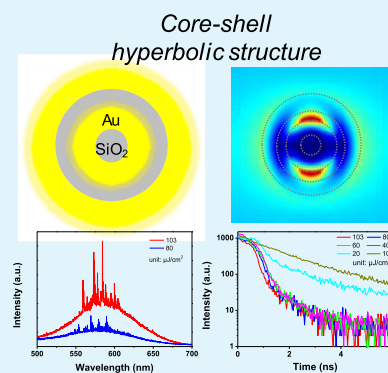
<sup>⊥</sup>Nanoscience and Nanotechnology Program, Taiwan International Graduate Program, Institute of Physics and <sup>#</sup>Research Center for Applied Sciences, Academia Sinica, Taipei 115, Taiwan

<sup>∇</sup>Institute of Optoelectronic Sciences, National Taiwan Ocean University, Keelung 202, Taiwan

## Supporting Information

**ABSTRACT:** Plasmonic material has emerged with multifunctionalities for its remarkable tailoring light emission, reshaping density of states (DOS), and focusing subwavelength light. However, restricted by its propagation loss and narrowband resonance in nature, it is a challenge for plasmonic material to provide a broadband DOS to advance its application. Here, we develop a novel nanoscale core–shell hyperbolic structure that possesses a remarkable coupling effect inside the multishell nanoscale composite owing to a higher DOS and a longer time of collective oscillations of the electrons than the plasmonic-based pure-metal nanoparticles. Subsequently, a giant localized electromagnetic wave of surface plasmon resonance is formed at the surface, causing pronounced out-coupling effect. Specifically, the nanoscale core–shell hyperbolic structure confines the energy well without being decayed, reducing the propagation loss and then achieving an unprecedented stimulated emission (random lasing action by dye molecule) with a record ultralow threshold ( $\sim 30 \mu\text{J}/\text{cm}^2$ ). Besides, owing to the radial symmetry of the nanoscale core–shell hyperbolic structure, the excitation of high wavevector modes and induced additional DOS are easily accessible. We believe that the nanoscale core–shell hyperbolic structure paves a way to enlarge the development of plasmonic-based applications, such as high optoelectronic conversion efficiency of solar cells, great power extraction of light-emitting diodes, wide spectra photodetectors, carrying the emitter inside the core part as quantitative fluorescence microscopy and bioluminescence imaging system for in vivo and in vitro research on human body.

**KEYWORDS:** hyperbolic structure, random lasers, core–shell nanoparticles, localized surface plasmon resonance, photonic density of states



## INTRODUCTION

Under light illumination on the noble-metal nanoparticles (NPs), surface plasmon polaritons (SPPs) can be excited as a form of the propagation wave at the surface owing to the coupling effect.<sup>1,2</sup> When these SPPs are spatially confined to the NPs resulting from the collective oscillation of electrons at their surfaces, localized surface plasmon resonance (LSPR) is known to boost the strength of electromagnetic field.<sup>3–5</sup> These phenomena are plasmonic-based concepts based on the modified density of states of light, which enables a great impact in the development of nanoscale science and technology.<sup>6</sup> To induce more LSPR, recently, core–shell NPs have been synthesized as the form of dielectric (core)–metal (shell), metal–dielectric, semiconductor–semiconductor, or other compositions for biomedicine, catalysis, controlling drug delivery, tissue engineering, and surface-

enhanced Raman scattering applications.<sup>7–10</sup> However, the above mentioned behaviors are limited by their natural loss and narrowband resonance that restrict to achieve a broadband and stronger LSPR or even go beyond the plasmonic effect. Therefore, overcoming the above difficulty still remains a great challenge.

Apart from the natural plasmonic property of metal NPs, metamaterials were derived from the existing natural materials and their combinations to achieve unnatural electromagnetic phenomena by tailoring their phases, amplitudes, and polarizations, such as metasurface,<sup>11</sup> hyperlens,<sup>12,13</sup> and metalens.<sup>14–16</sup> One of the most significant breakthrough is

**Received:** August 12, 2018

**Accepted:** December 13, 2018

**Published:** December 13, 2018

hyperbolic metamaterials (HMMs), with the unique hyperboloid of isofrequency contour in momentum–space bringing about unlimited wavevectors (high- $k$  modes) and subsequently increasing the photonic density of states (PDOS).<sup>17,18</sup> Moreover, these high- $k$  modes are realized as the volume plasmon polaritons emerged from the intercoupling effect of SPPs by the metal–dielectric interfaces.<sup>19,20</sup> Several intriguing developments have then been unveiled, including ultrahigh sensitive biosensors,<sup>21</sup> robustly enhanced fluorescence emission,<sup>22,23</sup> and increase in the charge-transfer dynamics for photonics, optoelectronics, and chemistry.<sup>24,25</sup> Considering the van der Waals heterostructures with atomic thickness, HMMs have been proven to assist the carriers transfer in between graphene and hexagonal boron nitride through a strong near-field coupling that opened a new era in nanoelectronics.<sup>26</sup> The HMMs are also employed to boost the transition rates of optical gain media to trigger the lasing action with higher possibility.<sup>27–30</sup> Additionally, the control of directivity for efficient deep-ultraviolet power extraction and high-speed optical transmission applications could be accomplished by artful design of HMMs.<sup>31,32</sup> To achieve these functionalities, previous methods have used patterned nanostructures through electron beam lithography or focused ion beam (FIB) technology to effectively couple out the energy, whereas they are too costly for commercialization.<sup>33,34</sup> Hyperbolic multilayered nanotube could be a solution because its structure is achievable from the self-roll-up process.<sup>35,36</sup> However, the drawback of this nanotube is that it does not have a truly three-dimensional (3D) symmetry, indicating only specific incident light direction (perpendicular to the surface) can induce its potential PDOS. To utilize these characteristics to extremes, the demand of unearthing novel metamaterials with a stronger LSPR effect and to conquer broad angular excitation from incident light is highly expected.

Here, we introduce the first nanoscale core–shell hyperbolic structure that possesses a superior plasmonic coupling effect inside the multishell structure and enables to generate a giant PDOS. Thus, the nanoscale core–shell hyperbolic structure can produce a stronger intensity of LSPR leading to the pronounced out-coupling effect. In addition, due to its naturally radial symmetry, the nanoscale core–shell hyperbolic structure makes the excitation of pronounced PDOS independent of the direction of incident light. Besides, the nanoscale core–shell hyperbolic structure sustains the longer time of coupling effect inside the multishell structure and then continuously couples the energy through the dielectric core material. One of the particular interests in stimulated emission is random laser. It is deemed as the succeeding light source by multiple scattering in between the disordered materials, making gain overcome its loss.<sup>37,38</sup> Benefits of broad angular emission, simple design, and easily accessible characteristics provide random laser system a great potential for display, biological probe, full-field microscopy, and white light illumination.<sup>38–42</sup> Furthermore, it is not required for a random laser system to hold a rigorous cavity.<sup>38,43,44</sup> Diversified functionalities have then been achieved, such as highly stretchable and flexible optoelectronics and dissolvable and recyclable random laser devices.<sup>45,46</sup> Therefore, for a proof-of-concept demonstration, we integrate the nanoscale core–shell hyperbolic structure with 4-(dicyanomethylene)-2-*tert*-butyl-6-(1,1,7,7-tetramethyljulolidin-4-yl-vinyl)-4*H*-pyran (DCJTb) dye molecule to achieve random laser action as a platform for stimulated emission. This random lasing action system

enables to achieve a record ultralow threshold ( $\sim 30 \mu\text{J}/\text{cm}^2$ ) due to the formation of closed loop paths by the highly scattered nanoscale core–shell hyperbolic structure. Three-dimensional finite-difference time-domain (FDTD) simulations verify our experimental results. Potential applications could be imaged when introducing the nanoscale core–shell hyperbolic structure, such as plasmonic nanoscale lasers, light-emitting diodes with high power extraction, and broadband absorption with tremendous photoelectric conversion efficiency for solar cells and photodetectors. Even more, the nanoscale core–shell hyperbolic structure can carry the quantum emitters inside the core as a quantitative fluorescence microscopy and bioluminescence imaging system for *in vivo* and *in vitro* researches on human body. Consequently, the nanoscale core–shell hyperbolic structure is promised to be useful for practical industrial applications due to its easily synthesized characteristic; thus, it is expected to be a rescue for exploring plasmonic-based technologies and metamaterials.

**Design, Characterization, and Optical Property of the Nanoscale Core–Shell Hyperbolic Structure.** The schematic diagram of nanoscale core–shell hyperbolic structure under light illumination is depicted in Figure 1a. This novel nanoscale core–shell hyperbolic structure is composed of the core material,  $\text{SiO}_2$  (silica), with a radius of 3 nm and

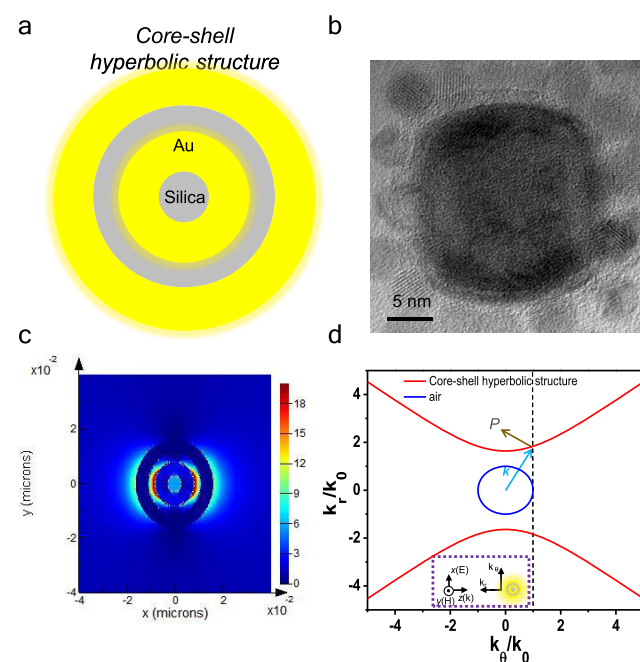


**Figure 1.** Proof-of-concept design of the nanoscale core–shell hyperbolic structure. (a) The schematic diagram of the nanoscale core–shell hyperbolic structure under light illumination to effectively excite the pronounced photonic density of states (PDOS). (b) Transmission electron microscopy (TEM) image of the nanoscale core–shell hyperbolic structure. The highly compact Au NPs form the layer for simulation. (c) The distributions of electric field intensity ( $|E|^2$ ) around the nanoscale core–shell hyperbolic structure. (d) Isofrequency contours of the nanoscale core–shell hyperbolic structure and air. Inset image is the schematic diagram of incident plane wave ( $\vec{k}$ ) and polarization direction ( $\vec{E}$ ) by a spherical coordinate.  $k$  represents the out-coupling wavevector and  $P$  is the Poynting vector that out-couples to the free space. The dashed line is the conservation of the  $k$ -vector component between the nanoscale core–shell hyperbolic structure and air.

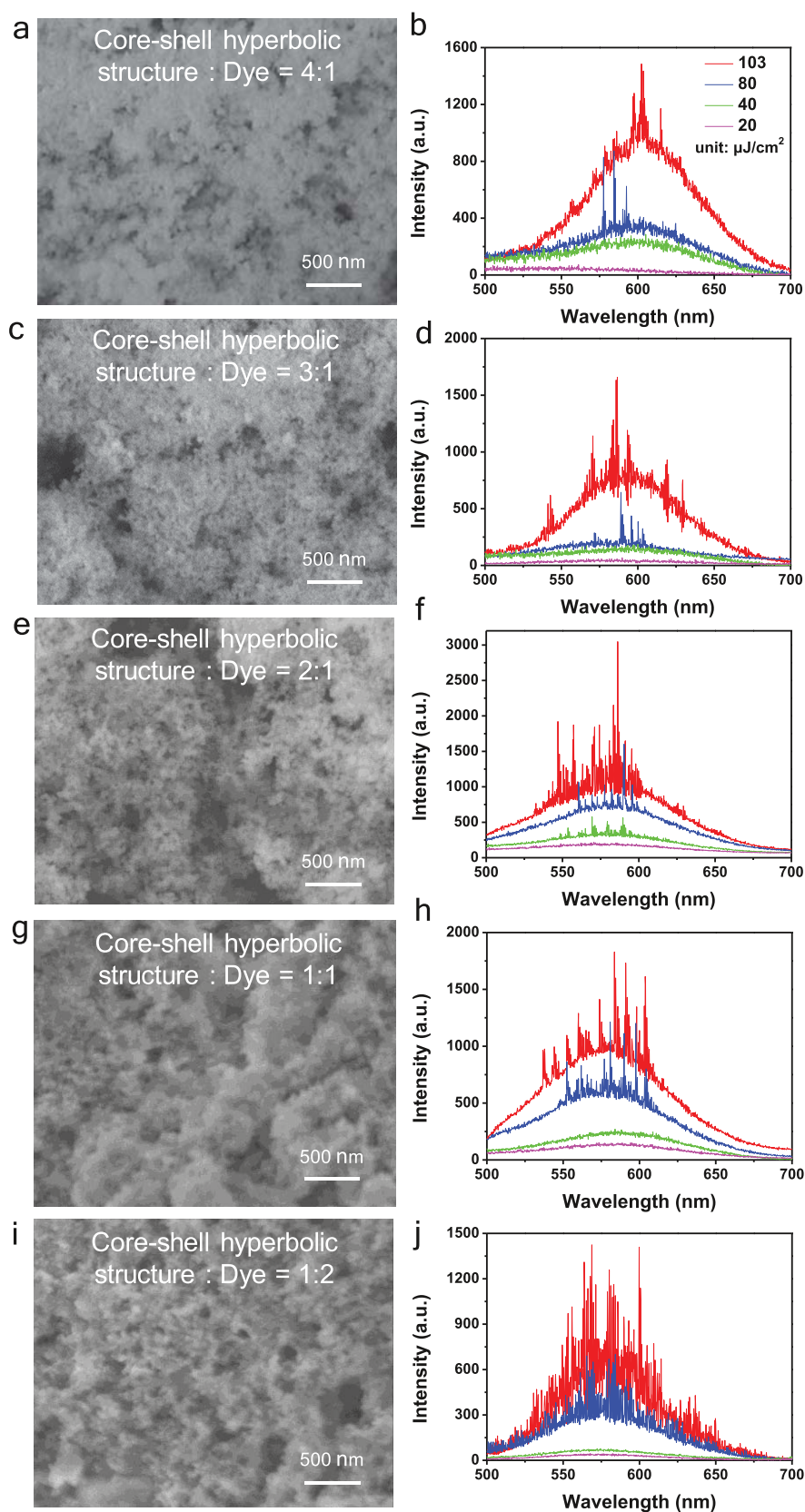


**Figure 2.** Random laser action based on the nanoscale core-shell hyperbolic structure. (a) The top-view scanning electron microscope (SEM) image of the nanoscale core-shell hyperbolic structure mixed with 4-(dicyanomethylene)-2-*tert*-butyl-6-(1,1,7,7-tetramethyljulolidin-4-yl-vinyl)-4*H*-pyran (DCJTB) dye molecules in a volume ratio of 4:1. (b) The corresponding emission spectra. All the emission spectra were excited by a 374 nm pulsed diode laser. ((c), (e), (g), and (i)) The SEM images in a volume ratio of 3:1, 2:1, 1:1, and 1:2, respectively. ((d), (f), (h), and (j)) The corresponding emission spectra.

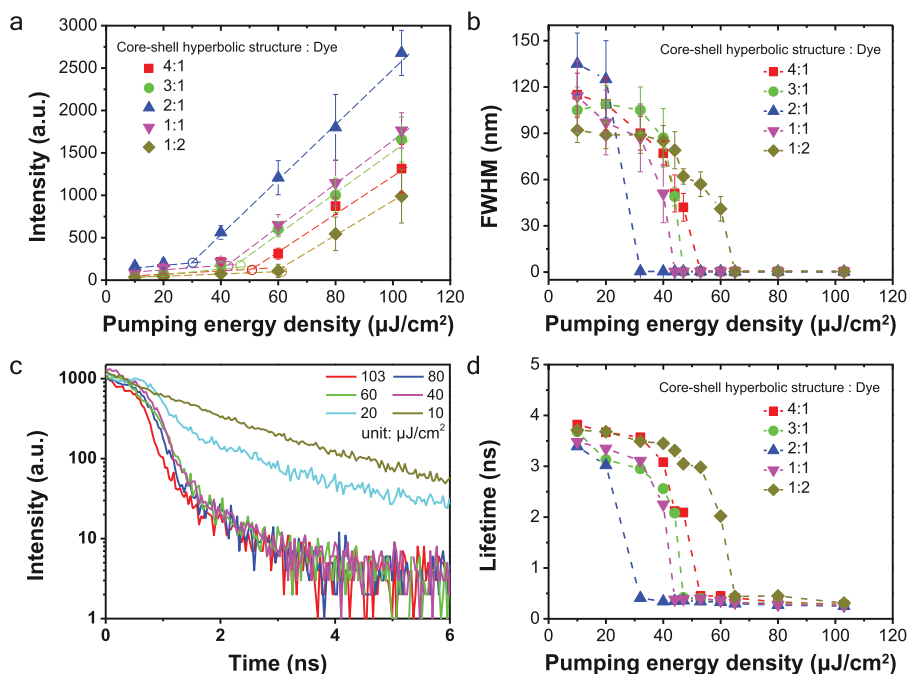


**Figure 3.** Characterization of random laser action. (a) The peak emission intensity as a function of pumping energy density. The fitted lines are the spontaneous emission (flat slope) and stimulated emission (sharp slope) with the threshold (hollow circle) of random lasing action of  $\sim 50$ , 47, 30, 42, and  $61 \mu\text{J}/\text{cm}^2$  in a volume ratio of 4:1, 3:1, 2:1, 1:1, and 1:2, respectively. (b) The full width at half-maximum (FWHM) as a function of pumping energy density. (c) The lifetime measurements for the samples with the volume ratio of 2:1. (d) The lifetime as a function of pumping energy density.

alternative multishells, and Au (5 nm)/silica (3 nm)/Au (5 nm). The total radius of the nanoscale core-shell hyperbolic structure is 16 nm. Figure 1b presents the transmission electron microscopy (TEM) image of the nanoscale core-shell hyperbolic structure. A detailed discussion of the TEM image is shown in Figure S1. Because the synthesis of silica-Au core-shell hyperbolic structure consists of several steps, measuring the  $\zeta$ -potential of each step of surface functionalization is one of the suitable methods to provide the additional evidence for the formation of the core-shell motifs as shown in Figure S2. To illustrate the importance of nanoscale core-shell hyperbolic structure, Figure S3 shows the silica@Au NP as a plasmonic-based reference, including Au (radius of 3 nm) as a core and silica (2 nm) as a shell layer. Figure 1c is the simulated cross-sectional electric field intensity ( $|E|^2$ ) distribution of the nanoscale core-shell hyperbolic structure using 3D FDTD method to realize the LSPR effect.

Considering the nanoscale core-shell hyperbolic structure, the thickness of each layer is much smaller than the operating wavelength and remains the same. Then, the effective dielectric tensor in radial direction is<sup>12,13</sup>

$$\epsilon_r = \frac{2\epsilon_{\text{Au}}\epsilon_{\text{SiO}_2}}{\epsilon_{\text{Au}} + \epsilon_{\text{SiO}_2}} \quad (1)$$

And, in polar and azimuth (tangential to the surface) directions, they can be expressed as

$$\epsilon_\theta = \epsilon_\phi = \frac{\epsilon_{\text{Au}} + \epsilon_{\text{SiO}_2}}{2} \quad (2)$$

where  $\epsilon$  is the permittivity. To further discuss the out-coupling configuration ( $|k_{\text{HMM}}| > |k_{\text{air}}|$ ) of the nanoscale core-shell hyperbolic structure, the isofrequency contour is shown in Figure 1d. Inset image depicts the corresponding spherical

coordinate. Considering the optical tensor, the different sign of permittivity is opposite ( $\epsilon_r \cdot \epsilon_\theta < 0$ ).<sup>13</sup> Thus, the dispersion relation changes from elliptical to hyperboloid as

$$\left(\frac{k_\theta}{k_0}\right)^2 \frac{1}{\epsilon_r} + \left(\frac{k_r}{k_0}\right)^2 \frac{1}{\epsilon_\theta} = 1 \quad (3)$$

where  $k_0 = \omega/c$  ( $\omega$  is the angular frequency and  $c$  is the speed of light in vacuum). The calculated effective permittivity of the metal-dielectric multishells with the thickness of  $\text{SiO}_2$  (3 nm)/Au (5 nm) is shown in Figure S4. With the negative component of effective permittivity ( $\epsilon_\theta$ ) above the wavelength regions of 450 nm, the metal-dielectric multishells can be deemed as hyperbolic dispersion. The emission spectra of random lasing action mixed with DCJTB dye molecules are within 500–700 nm, which can be influenced by the effect of hyperbolic dispersion as shown in our study. This distinction allows the existence of high- $k$  modes to assist wave propagation inside the multishell structure instead of being annihilated as a form of evanescent field, subsequently producing the remarkable PDOS as compared to the general materials with elliptical dispersion.

**Emission Dynamics.** To illustrate the usefulness of nanoscale core-shell hyperbolic structure, it is mixed with DCJTB dye molecules to demonstrate the random laser action as shown in Figure 2. Figure 2a presents the top-view scanning electron microscopy (SEM) image of the nanoscale core-shell hyperbolic structure mixed with 4-(dicyanomethylene)-2-*tert*-butyl-6-(1,1,7,7-tetramethyljulolidin-4-yl-vinyl)-4*H*-pyran (DCJTB) dye molecules in a volume ratio of 4:1. The sizes in irregular and randomly distributed mixtures ranged from tens of nanometers. These morphologies are beneficial for the formation of closed-loop paths to trap the light and then enlarge the optical gain by multiple scattering process, resulting

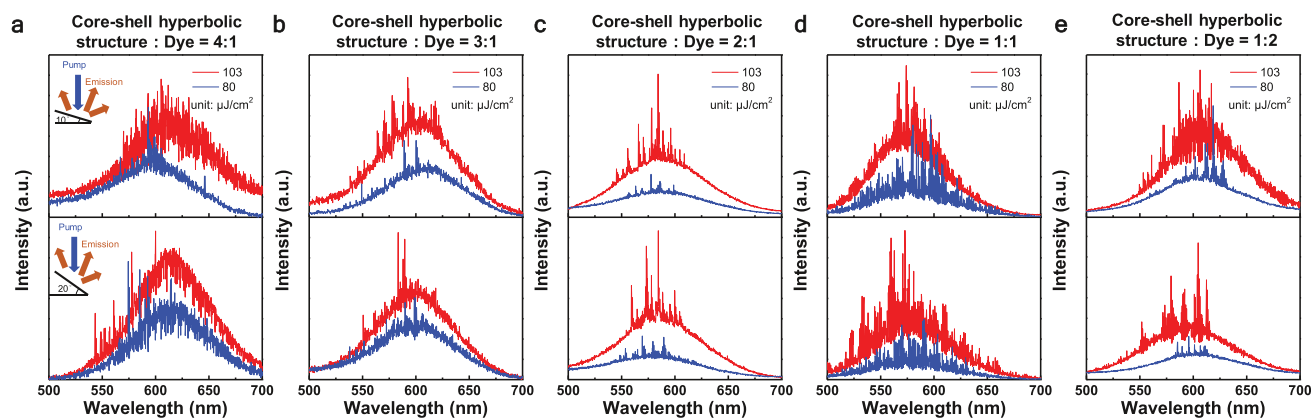


**Figure 4.** Broad angular emission. (a) The emission spectra of random lasing action detected at a tilted sample holder angle of  $10^\circ$  (upper) and  $20^\circ$  (bottom) for the volume ratio of 4:1. Inset image is the schematic diagram of tilted sample holder measurement. ((b), (c), (d), and (e)) The corresponding emission spectra for the volume ratio of 3:1, 2:1, 1:1, and 1:2, respectively. These broad angular emissions demonstrate the unique characteristic of the random laser action.

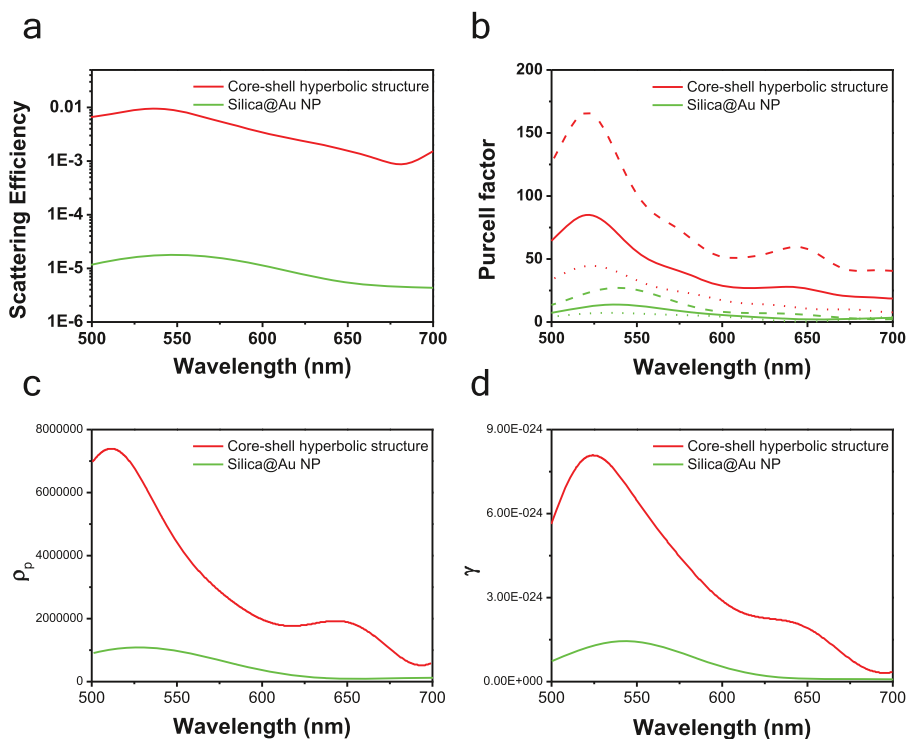


**Figure 5.** Theoretical analysis. (a) The scattering efficiency (scattering cross section divided by its scattering cross-sectional area). (b) The Purcell factor is an isotropic dipole ( $F_{\text{iso}}$ , marked as the solid line) with dipole sources perpendicular ( $F_{\perp}$ , marked as the dash line) and parallel ( $F_{\parallel}$ , marked as the dot line) to the surface for 10 nm to address the variation of emission rates around the environment. Furthermore, considering the light-matter interaction, the approach of dyadic Green's function is used to determine (c) the local density of states (LDOS) ( $\rho_p$ ) and (d) the spontaneous decay rate ( $\gamma$ ). All the simulation spectra are set at the wavelength region of 500–700 nm.

in the amplification of stimulated emission and the occurrence of random laser action. Figure 2b shows the corresponding emission spectra. Figure 2c,e,g,i are the SEM images in a volume ratio of 3:1, 2:1, 1:1, and 1:2, respectively, and Figure 2d,f,h,j are the corresponding emission spectra. Several sharp peaks with linewidths of  $\sim 0.3$  nm are clearly seen above the pumping energy densities. And, Figure 3a,b show the corresponding peak emission intensity and full width at half-maximum (FWHM) as a function of pumping energy density. Between a relative flat slope (spontaneous emission) and a sudden increase in shape slope (stimulated emission), the intersection (hollow circle) of these two lines is an ultralow

lasing threshold of  $\sim 50$ , 47, 30, 42, and  $61 \mu\text{J}/\text{cm}^2$ , respectively. Note that the lasing threshold of pumping energy density of  $30 \mu\text{J}/\text{cm}^2$  for the sample with the volume ratio of 2:1 outperforms all the values ever reported for the similar laser dye systems. Figure 3c is the lifetime measurements for the volume ratio of 2:1 and Figure 3d is the lifetime as a function of pumping energy density, whereas for the samples with other volume ratio, the lifetime measurements are shown in Figure S5. When achieving random lasing action, the lifetime shortens to  $\sim 0.25$  ns as compared with the spontaneous emission, which is larger than 3 ns.

The well-known randomly emerged lasing peaks are realized briefly as follows. When light passes through the highly scattered nanoscale core–shell hyperbolic structure with a strong energy confinement, it is able to trap the coherent photons well to form a closed loop path. Then, the optical gain is amplified, making gain overcome its loss easily, which triggers stimulated emission to achieve random laser action. Because the chances of forming closed loop paths are high, the lasing peaks with linewidths of  $\sim 0.3$  nm appear randomly at different measuring times. In our study, the optimized performance of lasing action is the volume ratio of 2:1. It can be realized by the fact that the concentration of the nanoscale core–shell hyperbolic structure can increase the possibility of the formation of closed loop path. When the nanoscale core–shell hyperbolic structure is too diluted, the number of the scattering events to form closed loops is much less (e.g., 1:1 and 1:2). However, for a larger volume ratio (e.g., 3:1 and 4:1), the possibility to generate these closed loop paths is also reduced due to the excessive densely packed NPs, which can produce too many scattering events and inhibit the formation of closed loops. Broad angular measurements of angles for 10 and 20° are shown in Figure 4, where the angle is between the normal vector and observing direction. Broad angular emission spectra were detected as a firm signature of random laser action in addition to the occurrence of threshold behaviors observed in emission spectra. In stark contrast, for mixture of silica@Au NPs and DCJTb dye molecules (Figures S6 and S7) and the pure DCJTb dye molecules (Figure S8), only the spontaneous emissions can be observed without any sign of lasing action. This measurement provides a further evidence of the important role played by the nanoscale core–shell hyperbolic structure in the observed laser action.

**Theoretical Analysis.** Next, let us discuss theoretically the functionalities of the nanoscale core–shell hyperbolic structure having a stronger plasmonic coupling effect than silica@Au NPs. Figure 5 demonstrates the simulated cross-sectional  $|E|^2$  distributions using 3D FDTD method to realize the LSPR effect of transverse magnetic and transverse electric modes. The maximum  $|E|^2$  profile at the core position for the nanoscale core–shell hyperbolic structure shows  $\sim 9.3$  times higher intensity than silica@Au NP, whose intensity is more than 10 times stronger at the nearest interface of Au and silica. This is due to the strong coupling effect triggered by the high- $k$  modes inside the multishell structure of the nanoscale core–shell hyperbolic structure to sustain the longer time of energy propagation rather than being annihilated owing to Ohmic loss. Figure S9 illustrates the 3D components of  $|E_x|^2$ ,  $|E_y|^2$ , and  $|E_z|^2$  using a normally incident light at wavelength of 590 nm around the nanoscale core–shell hyperbolic structure and silica@Au NP. As anticipated, the nanoscale core–shell hyperbolic structure out-couples  $|E|^2$  to the free space. Movie S1 depicts the time-resolved  $|E|^2$  distributions to support our proposed mechanism.

To develop the interaction between LSPR and the nanoscale core–shell hyperbolic structure, the discussion of Mie scattering theory is necessary.<sup>47</sup> Note that the scattering process of light plays an important role in out-coupling the energy to the environment instead of being annihilated as an evanescent field. To out-couple the energy to the far-field or extract light directivity, previous reports have integrated the nanopatterned hyperbolic structures with sophisticated design using FIB or electron beam lithography.<sup>21,22,34</sup> However, for the large-area fabrication and upcoming industrial applications,

these methods are too ineffective. In this study, the nanoscale core–shell hyperbolic structure can be considered as more suitable and effective for large-area fabrication than the above-mentioned methods to couple out energy or achieve strong light–matter interaction. This is due to the fact that the formation of the core–shell hyperbolic structure is in the solution form, which can be easily mixed with the dye molecules or the gain medium for the purpose of light-emitting diode, solar cells, and even achieving the lasing action, as we have demonstrated in this study. Besides, the core–shell hyperbolic structure can be also easily spin-coated on the substrate for the multijunction photodetectors applications with high electronic–optical conversion efficiency.

Figure S10 presents the radiation patterns for the nanoscale core–shell hyperbolic structure and silica@Au NP, demonstrating that these two structures have radial symmetry in 3D space. Prominently, the nanoscale core–shell hyperbolic structure is suitable for a large-area fabrication and angle-free incident of light to excite pronounced PDOS. Figure 5a shows the scattering efficiency (scattering cross section ( $\sigma_{\text{scat}}$ ) divided by its scattering cross-sectional area ( $A_{\text{scat}}$ )).<sup>47</sup> Detailed calculation method is discussed in the Supporting Information. At the emission wavelength center (590 nm) for DCJTb dye molecule, the scattering efficiency for the nanoscale core–shell hyperbolic structure is significantly  $\sim 320$  times higher than that of silica@Au NP. This higher scattering efficiency results from the strong coupling effect between the multishell structure with lower propagation dissipation. High scattering of the nanoscale core–shell hyperbolic structure is observed at different incident angle ( $\theta$ ) from normal ( $0^\circ$ ) to  $50^\circ$  as shown in Figure S11. In the end, this strong coupling effect out-couples the energy to the surrounding dye molecules well to drastically enhance the random lasing action.

We further calculated the Purcell factor ( $F_{\text{iso}}$ ) to express the variation of spontaneous emission rates around the environment, which is composed of the dipole orientations perpendicular ( $F_{\perp}$ ) and parallel ( $F_{\parallel}$ ) to the substrate as<sup>22,48</sup>

$$F_{\text{iso}} = \frac{1}{3}F_{\perp} + \frac{2}{3}F_{\parallel} \quad (4)$$

Figure 5b presents the Purcell factor with dipole sources above the outermost surface for 10 nm in a wavelength region of 500–700 nm, whereas Figure S12 is the dipole distance within 50 nm marked in a logarithmic scale to emphasize the importance of the near-field coupling effect. At the emission center for DCJTb dye molecule at 590 nm, the Purcell factor for the nanoscale core–shell hyperbolic structure is  $\sim 5$  times higher than that for the silica@Au NP. The underlying mechanism is explained based on the Fermi's golden rule. Considering the quantum mechanism, the transition rate ( $\Gamma_{\text{fi}}$ ) from the initial state ( $\Psi_i$ ) to the final state ( $\Psi_f$ ) is given by<sup>49</sup>

$$\Gamma_{\text{fi}} = \frac{2\pi}{\hbar} |\langle \Psi_f | H | \Psi_i \rangle|^2 \rho(k) \quad (5)$$

where  $\hbar$  is the Dirac's constant,  $\langle \Psi_f | H | \Psi_i \rangle$  is the matrix component of the inner product perturbation Hamiltonian ( $H$ ) from  $\Psi_i$  to  $\Psi_f$ , and  $\rho(k)$  is the density of final states that is proportional to  $k^3$ . The nanoscale core–shell hyperbolic structure has unlimited wavevectors compared to the bounded value for the isotropic medium, leading to the higher transition rate. Therefore, the nanoscale core–shell hyperbolic structure possesses a pronounced PDOS.

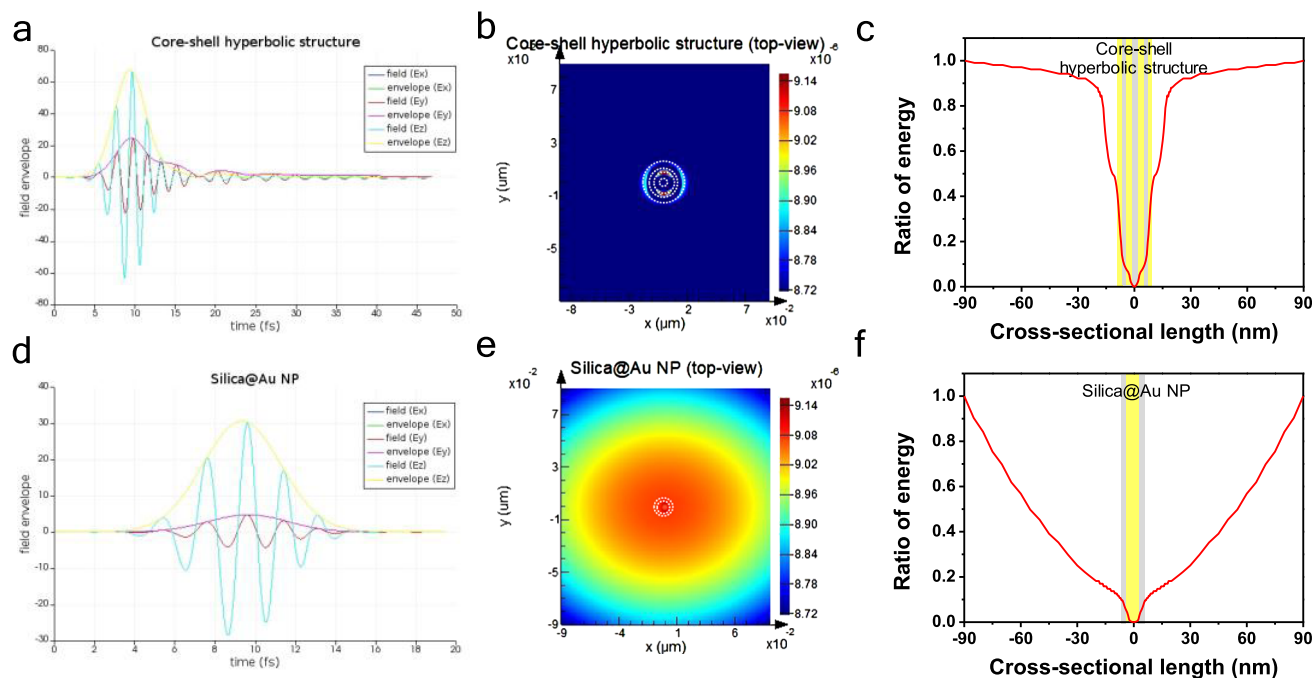


**Figure 6.** Optical characterizations. (a) The time decay of field components with the corresponding envelopes for the nanoscale core–shell hyperbolic structure. (b) The energy distributions of the top-view profiles for the nanoscale core–shell hyperbolic structure. (c) The ratio of energy for the nanoscale core–shell hyperbolic structure. (d) The time decay of field components with the corresponding envelopes for the silica@Au NP. (e) The energy distributions of the silica@Au NP. (f) The ratio of energy for the silica@Au NP. The mode volume for nanoscale core–shell hyperbolic structure (silica@Au NP) is simulated as  $176\ 159\ (215\ 980)\ \text{nm}^3$ . The nanoscale core–shell hyperbolic structure can confine the energy well without being decayed, reduce the propagation loss, and then trigger the lasing action.

Furthermore, considering the light–matter interaction in a two-level quantum system, we calculated the local density of states (LDOS) (in Figure 5c) and spontaneous decay rate ( $\gamma$ ) (in Figure 5d) from the approach of dyadic Green's function ( $G(r_0, r_0; \omega_0)$ ). At point  $r = r_0$  and  $\omega = \omega_0$  along the  $p$  direction generates electric field, where  $r$  is the position coordinate and  $\omega$  is its frequency.<sup>50</sup> Thus, the LDOS is determined by

$$\rho_p(r_0, \omega_0) = \frac{6\omega_0}{\pi c^2} [n_p \cdot \text{Im}\{G(r_0, r_0; \omega_0)\} \cdot n_p] \quad (6)$$

and the spontaneous decay rate by

$$\gamma = \frac{\pi\omega_0}{3\hbar\epsilon_0} |p|^2 \rho_p(r_0, \omega_0) \quad (7)$$

Note that  $\gamma$  is related to  $\rho_p$ , demonstrating that a photon with energy of  $\hbar\omega_0$  is emitted through a process of spontaneous decay for number of modes per unit volume at the specific frequency. As expected, both the LDOS and spontaneous decay rate for the nanoscale core–shell hyperbolic structure are  $\sim 4.8$  times higher than that of the silica@Au NP due to the pronounced PDOS that can also be used to support our proposed mechanism. To have a more detailed examination of the measured spectra, a slight blue shift is observed for the volume ratio of 2:1. This is caused by the dispersion of the Purcell factor and the density of photonic states.<sup>51–54</sup> Therefore, benefiting from the proper concentration of the nanoscale core–shell hyperbolic structure, the strongest lasing intensity occurred at the optimized volume ratio of 2:1, which is in good agreement with our observation. We further simulated the theoretical analyses for the refractive index of Au for nanoscale materials and the literature values for bulk

materials, as shown in Figure S13. The observed trends are similar with less discrepancy.

The nanoscale core–shell hyperbolic structure sustains the longer time and strength of coupling effect, which is  $\sim 2.2$  ( $3.9$ ) times higher than that of silica@Au NP for the field envelop (Figure 6a,d). To consolidate the nanoscale core–shell hyperbolic structure to trigger a lasing action, we consider the Purcell factor as another form of<sup>55</sup>

$$F_{\text{iso}} = \frac{3}{4\pi^2} \left( \frac{\lambda_c}{n_c} \right)^3 \left( \frac{Q}{V_{\text{eff}}} \right) \quad (8)$$

where  $\lambda_c$  is the wavelength in free space,  $n_c$  is the refractive index at the dipole position,  $Q$  is the quality factor ( $Q$ -factor), and  $V_{\text{eff}}$  is the effective mode volume. To further develop the light–matter interaction, we discuss the  $Q$ -factor and  $V_{\text{eff}}$  for the nanoscale core–shell hyperbolic structure. The  $Q$ -factor is defined by the resonance wavelength ( $\lambda$ ) divided by its FWHM ( $\Delta\lambda$ )

$$Q = \frac{\lambda}{\Delta\lambda} \quad (9)$$

and mode volume<sup>52,56,57</sup>

$$V_{\text{eff}} = \frac{\iiint W(r') d^3(r')}{\max W(r')} \quad (10)$$

$$W(r') = \frac{1}{2} \text{Re} \left\{ \frac{d[\omega\epsilon(r')]}{d\omega} \right\} |\vec{E}(r')|^2 + \frac{1}{2} \mu_0 |\vec{H}(r')|^2 \quad (11)$$

where  $W(r')$  is the energy density of the NP in free space. Fundamentally, a larger  $Q$ -factor represents the longer time that the electromagnetic wave can sustain inside the nanoscale

core–shell hyperbolic structure without being totally decayed or leaked out.<sup>55,58</sup> A small  $V_{\text{eff}}$  means that the electromagnetic wave can be confined inside a small volume, thus reducing the propagation loss to enhance the emission.<sup>55,58</sup> A reduction of mode volume represents the shortened paths of closed loop, which provides an excellent platform to trigger random laser action with a higher possibility.<sup>58–60</sup> The energy density of these closed loop paths are higher, resulting in the stronger localized field. The transition probability for the nearby dye material is subsequently enhanced, then the emission of the random laser action is easily achieved. The  $Q$ -factor for the nanoscale core–shell hyperbolic structure (silica@Au NP) from the experimental result is  $\sim 2000$  (5). This high  $Q$ -factor is due to the fact that the random lasing action arises from the unique characteristics of the nanoscale core–shell hyperbolic structure. In comparison, the  $V_{\text{eff}}$  for the nanoscale core–shell hyperbolic structure and silica@Au NP is calculated to have a value of 176 159 and 215 980 nm<sup>3</sup>, respectively. Figure 6b (S14a) and 6e (S14b) show the corresponding energy distributions of the top-view (cross-sectional) profiles, respectively. We simulated the ratio of energy for the nanoscale core–shell hyperbolic structure (Figure 6c) and the silica@Au NP (Figure 6f) as the quantitative results to realize the distributions of energy. Within the radius of nanoscale core–shell hyperbolic structure (16 nm), the ratio of energy that can be stored is  $\sim 30\%$ , even reaching  $\sim 90\%$  at the cross-sectional length of 44 nm, showing that the nanoscale core–shell hyperbolic structure is able to confine the energy well. Therefore, the propagation loss is reduced, which enables to provide a strong feedback to achieve the lasing action. On the contrary, for the silica@Au NP, within the radius of 5 nm, the ratio of energy that can be stored is  $\sim 1.2\%$ , and reached only  $\sim 19\%$  at the cross-sectional length of 44 nm, which implies that the plasmonic-based reference sample is not able to store the energy with higher efficiency. The random laser action is a multiple scattering process from the nanoscale core–shell hyperbolic structure that produces a low loss and high energy confinement surroundings to make the “lucky photons” enable to boost the light–matter interaction to achieve random lasing action. Considering Au/silica as a multilayer thin film component, the  $V_{\text{eff}}$  is calculated to be 36 553 200 nm<sup>3</sup>. The corresponding time decay of the field envelope component and the energy distributions are shown in Figure S15. Note that the mode volume is  $\sim 208$  times larger than that of the nanoscale core–shell hyperbolic structure, demonstrating that the energy is highly dissipated within the pure multilayer thin film structure.

**Perspectives.** Finally, we stress here that the main purpose of our current study is to demonstrate the proof-of-concept that the newly designed composite silica/gold metaparticles can be used to enhance the light–matter coupling and effectively reduce the lasing threshold, which is very useful for the further development of high-performance optoelectronic devices. Certainly, it is anticipated that with the increasing number of pairs of the nanoscale core–shell hyperbolic structure, the effect of core–shell hyperbolic structure NPs can be enhanced. For example, Figure S16 shows the scattering efficiency, Figure S17 presents the  $|E|^2$  distribution and Figure S18 shows the corresponding Purcell factor, LDOS, and the spontaneous decay rate. We can clearly see that the nanoscale core–shell hyperbolic structure demonstrates enhanced outstanding characteristics. Therefore, the nanoscale core–shell hyperbolic structure is expected to be

a succeeding research highlight in nano-optics that goes beyond the plasmonic effect. Since the above novel and irreplaceable properties of pronounced PDOS, potential prospects are attempting imagined. First, if the nanoscale core–shell hyperbolic structure is composed of biocompatible materials, it can be implanted in a human body for in vivo photothermal therapy or tumor imaging. Second, owing to the broadband enhancement of PDOS covering a wide spectral range, the nanoscale core–shell hyperbolic structure is suggested for highly efficient optoelectronic devices, such as solar cells and photodetectors. Moreover, because of the longer time of plasmonic coupling effect, the nanoscale core–shell hyperbolic structure promises to increase the hot-carrier-induced chemical reactions from the adsorbates or photo-degradation of organic pollutants. Interestingly, the nanoscale core–shell hyperbolic structure is even suitable for next-generation drug delivery concept or core-carrying emitters for quantitative fluorescence microscopy and bioluminescence imaging system by in vivo and in vitro researches on specimens, small animals, and human body. Supporting Information Movie S2 demonstrates the core-carrying emitter with a dipole source, as well as the corresponding Purcell factor at the center core (Figure S19). Furthermore, due to the radial symmetry of the nanoscale core–shell hyperbolic structure, the broad angular incident light can easily excite the high- $k$  modes and make PDOS higher, which can overcome the difficulty of light extraction due to its uniqueness of high directivity of the dispersion relation from the hyperbolic structure. This natural characteristic is deemed as a significant advancement for light-emitting diodes and laser technology. We therefore believe that our work shown here can lead a promising guideline for future developments in advanced optoelectronic devices with a wide variety of application.

## CONCLUSIONS

We have made a successful demonstration of the nanoscale core–shell hyperbolic structure composed of nanoscale silica as the core and Au/silica as multishell components. Interestingly, with its unique features, the nanoscale core–shell hyperbolic structure enables to achieve random laser action of DCJTB dye molecules with a record ultralow threshold of  $\sim 30 \mu\text{J}/\text{cm}^2$  in a volume ratio of 2:1. Confirmed by FDTD simulation results, the nanoscale core–shell hyperbolic structure plays an important role as a scattering center and induces pronounced LSPR effect owing to a significant increment of scattering efficiency ( $\sim 320$  times) compared with the reference Au NP sample. The nanoscale core–shell hyperbolic structure can confine the energy well, reduce the propagation loss, and provide the strong feedback to achieve lasing action. In addition, the simulation shows an increased Purcell factor, LDOS, and decay rates of about 5 times, demonstrating a higher PDOS nearby the nanoscale core–shell hyperbolic structure. It is believed that our demonstration not only enables to enlarge the developments in metamaterials but also invokes a new path in plasmonic-based applications, such as highly optoelectronic conversion efficiency of solar cells, large power extraction of light-emitting diodes, and wide spectral absorption of photodetectors.

**Materials and Methods.** NH<sub>4</sub>OH (25% aqueous solution), ethanol (99.5%), tetraethyl orthosilicate (TEOS, 95%), trisodium citrate dihydrate (Na-cit, 99%), HAuCl<sub>4</sub> (98%), and mercaptopropyl trimethoxy silane (denoted as MPTMS) were purchased from Sigma-Aldrich.

**Synthesis of Silica NPs.** Silica NPs were synthesized using the well-known Stober's method with simple hydrolysis and condensation reaction.<sup>61</sup> In the procedure, we have mixed concentrated ammonia solution (28%) with deionized water (9.0 mL) and absolute ethanol (27.0 mL) and mixture was sonicated for 30 min. Then, TEOS (2.4 mL) in absolute ethanol (50.0 mL) was added in this mixture and sonicated for a further 2 h to get a white turbid suspension. All the above experiments were conducted at room temperature. The mixture was then centrifuged at 10 000 rpm for 15 min after which the supernatant was removed and the solid pellet recovered.

**Surface Modification of Silica NPs.** Silica NPs were functionalized with mercaptopropyl trimethoxy silane (denoted as MPTMS) to introduce thiol groups (–SH) on their surface (referred to as SH@silica NPs). In the protocol, silica NPs (10 mg) were suspended in 10 mL of ethanol to which MPTMS was added (100  $\mu$ L) and stirred for 24 h at room temperature. The solution is rinsed using distilled ethanol followed by centrifugation (10 000 rpm) in ethanol.

**Synthesis of Au NPs.** We have employed the reduction of Au salt with Na-cit for Au NPs synthesis.<sup>62</sup> In the protocol, to the freshly prepared 0.94 mL of 0.34 M Na-citrate in H<sub>2</sub>O was added 200 mL of 0.24 mM HAuCl<sub>4</sub> in H<sub>2</sub>O at a constant temperature of 65 °C under vigorous stirring. The presence of Au NPs was indicated within a few minutes, with the solution turning wine red.

**Au Layer Immobilized on Silica NP (Au@Silica Core–Shell Structure).** Ten milligrams of SH@silica NPs was mixed with ethanol (10 mL) and then ultrasonicated for 30 min. One hundred of milligrams of Au NPs was added and sonicated for 30 min. Then, the reaction mixture was stirred vigorously for 12 h, so that Au NPs could be adsorbed on SH@silica NPs because Au has a higher affinity than thiol group. Later, the reaction mixture was precipitated by ethanol followed by centrifugation (10 000 rpm) in ethanol.

**Synthesis of Silica Layer on Au@Silica Core–Shell Structure (Silica–Au@Silica NPs).** The Au@silica core–shell structures were coated with tetraethyl orthosilicate (TEOS) to obtain a uniform and thin silica layer. For the nomenclature in this work, we have cited other published reports, which also used Au@silica as the same nomenclature to back up our usage.<sup>10,63</sup> Later, 80  $\mu$ L of ammonium hydroxide was added into the same solution mixture and sonicated for next 30 min. In the last step, 15  $\mu$ L of TEOS was added and the solution mixture was stirred for 24 h. Finally, the solution was precipitated by acetone and isolated via centrifugation. The pellets were washed twice with an ethanol/water (1:1) mixture to remove impurities.

**Coating of Second Au Layer on Silica-Coated Au Core–Shell Structure (Au@silica–Au@silica).** We have followed the earlier steps to coat the Au layer. Silica–Au@silica was functionalized with MPTMS to introduce thiol groups (–SH) on the silica NPs surface (referred to as SH@silica–Au@silica NPs). In the protocol, silica–Au@silica NPs structures (10 mg) were suspended in 10 mL of ethanol, to which MPTMS was added (100  $\mu$ L) and stirred for 24 h at room temperature. The solution was rinsed using distilled ethanol followed by centrifugation (10 000 rpm) in ethanol. Then, 10 mg of SH@silica–Au@silica core–shell NPs was mixed with ethanol (10 mL) and ultrasonicated for 30 min. One hundred milligrams of Au NPs was added and sonicated for 30 min. Then, the reaction mixture was stirred vigorously

for 12 h. Later, the reaction mixture was precipitated by ethanol followed by centrifugation (10 000 rpm) in ethanol.

**Instrumentation Detail of TEM.** Electron microphotographs were recorded on a JEOL JEM-1400 (120 kV) TEM.

**Preparation of DCJTB Dye Materials.** The DCJTB dye molecule was dissolved in dichloromethane with a concentration of 5 mg/mL at room temperature. These solutions were prepared with alcohol to mix with the nanoscale core–shell hyperbolic structure and Au NP. We stirred these solutions for 1 h at room temperature to obtain homogeneous mixtures. Afterward, we spin-coated the solutions on the precleaned Si substrates ( $\sim 1.5 \times 1.5$  cm), which were ultrasonically cleaned for 20 min in acetone, ethanol, and then deionized water to remove the contaminants. Finally, these samples were baked at 50 °C for 30 min on a hotplate to totally remove the deionized water or alcohol from these thin film.

**Mixture of the NPs with DCJTB Dye Materials.** The NPs solutions were mixed with DCJTB dye materials in volume ratios of 4:1 (48:12  $\mu$ L), 3:1 (45:15  $\mu$ L), 2:1 (40:20  $\mu$ L), 1:1 (30:30  $\mu$ L), and 1:2 (20:40  $\mu$ L) to compare the emission dynamics of the mixture influenced by the wavelength-dependent DOS.

**Measurement of Emission Dynamics.** We used a pulsed diode laser (Picoquant, PDL 800-B, center wavelength of 374 nm, 70 ps, 2.5 MHz) to measure the photoluminescence spectra and random lasing action, which were collected by a Horiba Jobin Yvon TRIAX 320 spectrometer. All the measurements of emission dynamics were performed at room temperature.

**Numerical Simulation.** The numerical simulation results were performed using a commercial electromagnetic software (Lumerical) of FDTD Solutions. The refractive index of silica with 1.45 was used and Au was from Pelik. All the simulation boundary conditions were confined by the perfectly matched layers to prevent the unavoidable results within the simulation region. All the mesh size of the computational region was set to be 0.1 nm.

## ■ ASSOCIATED CONTENT

### 📄 Supporting Information

The Supporting Information is available free of charge on the ACS Publications website at DOI: 10.1021/acsami.8b13844.

Time-resolved  $|E|^2$  distributions (AVI)

Core-carrying emitter with a dipole source (AVI)

Lifetime dynamics; spontaneous emission from DCJTB dye molecules and mixed with silica@Au NPs; distributions of  $|E|^2$ ; radiation pattern; simulation method of scattering efficiency; scattering cross section at different incident angles; Purcell factor within 50 nm away from the surface of NP; optical properties for the same thickness of Au/silica as a multilayer thin-film structure; simulation of  $|E|^2$  distributions for multipairs of nanoscale core–shell hyperbolic structure; simulation of spontaneous emission dynamics for multipairs of nanoscale core–shell hyperbolic structure; Purcell factor of the core-carrying emitter at the center core (PDF)

## ■ AUTHOR INFORMATION

### Corresponding Author

\*E-mail: yfchen@phys.ntu.edu.tw.

### ORCID

Hung-I Lin: 0000-0001-9849-3138

Golam Haider: 0000-0001-5300-3764

Monika Kataria: 0000-0003-4912-340X

Yit-Tsong Chen: 0000-0002-6204-8320

### Author Contributions

<sup>○</sup>H.-I.L. and K.Y. contributed equally to this work.

### Author Contributions

H.-I.L. and Y.-F.C. conceived the idea of nanoscale core–shell hyperbolic structure. K.Y. synthesized the nanoscale core–shell hyperbolic structure and took TEM images. H.-I.L., K.-C.S., G.H., T.-J.C., Y.-H.L., T.-Y.L., and Y.-F.C. discussed the mechanism of nanoscale core–shell hyperbolic structure. M.K. prepared DCJT dye molecule. P.K.R. took the SEM images. H.-I.L. measured emission spectra and performed simulation. H.-I.L., G.H., T.-Y.L., and Y.-F.C. discussed the mechanism of random laser action. Y.-F.C. supervised the project. H.-I.L., Y.-T.C., and Y.-F.C. wrote the paper. All the authors were involved in analyzing the data.

### Funding

This work was financially supported by the “Advanced Research Center for Green Materials Science and Technology” from The Featured Area Research Center Program within the framework of the Higher Education Sprout Project by the Ministry of Education (107L9006) and the Ministry of Science and Technology in Taiwan (MOST 107-3017-F-002-001).

### Notes

The authors declare no competing financial interest.

## ACKNOWLEDGMENTS

This work was financially supported by the “Advanced Research Center for Green Materials Science and Technology” from The Featured Area Research Center Program within the framework of the Higher Education Sprout Project by the Ministry of Education (107L9006) and the Ministry of Science and Technology in Taiwan (MOST 107-3017-F-002-001).

## REFERENCES

- (1) Anker, J. N.; Hall, W. P.; Lyandres, O.; Shah, N. C.; Zhao, J.; Van Duyne, R. P. Biosensing with Plasmonic Nanosensors. *Nat. Mater.* **2008**, *7*, 442–453.
- (2) Brongersma, M. L.; Halas, N. J.; Nordlander, P. Plasmon-Induced Hot Carrier Science and Technology. *Nat. Nanotechnol.* **2015**, *10*, 25–34.
- (3) Mayer, K. M.; Hafner, J. H. Localized Surface Plasmon Resonance Sensors. *Chem. Rev.* **2011**, *111*, 3828–3857.
- (4) Willets, K. A.; Duyn, R. P. V. Localized Surface Plasmon Resonance Spectroscopy and Sensing. *Annu. Rev. Phys. Chem.* **2007**, *58*, 267–297.
- (5) Hutter, E.; Fendler, J. H. Exploitation of Localized Surface Plasmon Resonance. *Adv. Mater.* **2004**, *16*, 1685–1706.
- (6) Boriskina, S. V.; Ghasemi, H.; Chen, G. Plasmonic Materials for Energy: From Physics to Applications. *Mater. Today* **2013**, *16*, 375–386.
- (7) Zhong, C. J.; Maye, M. M. Core-Shell Assembled Nanoparticles as Catalysts. *Adv. Mater.* **2001**, *13*, 1507–1511.
- (8) Gawande, M. B.; Goswami, A.; Asefa, T.; Guo, H.; Biradar, A. V.; Peng, D.-L.; Zboril, R.; Varma, R. S. Core-Shell Nanoparticles: Synthesis and Applications in Catalysis and Electrocatalysis. *Chem. Soc. Rev.* **2015**, *44*, 7540–7590.
- (9) Ghosh Chaudhuri, R.; Paria, S. Core/Shell Nanoparticles: Classes, Properties, Synthesis Mechanisms, Characterization, and Applications. *Chem. Rev.* **2012**, *112*, 2373–2433.
- (10) Kataria, M.; Yadav, K.; Haider, G.; Liao, Y. M.; Liou, Y.-R.; Cai, S.-Y.; Lin, H.-i.; Chen, Y. H.; Paul Inbaraj, C. R.; Bera, K. P.; Lee, H. M.; Chen, Y.-T.; Wang, W.-H.; Chen, Y. F. Transparent, Wearable,

Broadband, and Highly Sensitive Upconversion Nanoparticles and Graphene-Based Hybrid Photodetectors. *ACS Photonics* **2018**, *5*, 2336–2347.

(11) Wang, S.; Wu, P. C.; Su, V.-C.; Lai, Y.-C.; Hung Chu, C.; Chen, J.-W.; Lu, S.-H.; Chen, J.; Xu, B.; Kuan, C.-H.; Li, T.; Zhu, S.; Tsai, D. P. Broadband Achromatic Optical Metasurface Devices. *Nat. Commun.* **2017**, *8*, No. 187.

(12) Rho, J.; Ye, Z.; Xiong, Y.; Yin, X.; Liu, Z.; Choi, H.; Bartal, G.; Zhang, X. Spherical Hyperlenses for Two-Dimensional Sub-Diffractive Imaging at Visible Frequencies. *Nat. Commun.* **2010**, *1*, No. 143.

(13) Lu, D.; Liu, Z. Hyperlenses and Metalenses for Far-Field Super-Resolution Imaging. *Nat. Commun.* **2012**, *3*, No. 1205.

(14) Khorasaninejad, M.; Chen, W. T.; Zhu, A. Y.; Oh, J.; Devlin, R. C.; Rousso, D.; Capasso, F. Multispectral Chiral Imaging with a Metalens. *Nano Lett.* **2016**, *16*, 4595–4600.

(15) Chen, W. T.; Zhu, A. Y.; Khorasaninejad, M.; Shi, Z.; Sanjeev, V.; Capasso, F. Immersion Meta-Lenses at Visible Wavelengths for Nanoscale Imaging. *Nano Lett.* **2017**, *17*, 3188–3194.

(16) Khorasaninejad, M.; Chen, W. T.; Devlin, R. C.; Oh, J.; Zhu, A. Y.; Capasso, F. Metalenses at Visible Wavelengths: Diffraction-Limited Focusing and Subwavelength Resolution Imaging. *Science* **2016**, *352*, 1190–1194.

(17) Poddubny, A.; Iorsh, I.; Belov, P.; Kivshar, Y. Hyperbolic Metamaterials. *Nat. Photonics* **2013**, *7*, 948–957.

(18) Ferrari, L.; Wu, C.; Lepage, D.; Zhang, X.; Liu, Z. Hyperbolic Metamaterials and Their Applications. *Prog. Quantum Electron.* **2015**, *40*, 1–40.

(19) Zhukovsky, S. V.; Kidwai, O.; Sipe, J. E. Physical Nature of Volume Plasmon Polaritons in Hyperbolic Metamaterials. *Opt. Express* **2013**, *21*, 14982–14987.

(20) Vasilantonakis, N.; Nasir, M. E.; Dickson, W.; Wurtz, G. A.; Zayats, A. V. Bulk Plasmon-Polaritons in Hyperbolic Nanorod Metamaterial Waveguides. *Laser Photonics Rev.* **2015**, *9*, 345–353.

(21) Sreekanth, K. V.; Alapan, Y.; Elkabbash, M.; Ilker, E.; Hinczewski, M.; Gurkan, U. A.; De Luca, A.; Strangi, G. Extreme Sensitivity Biosensing Platform Based on Hyperbolic Metamaterials. *Nat. Mater.* **2016**, *15*, 621–627.

(22) Lu, D.; Kan, J. J.; Fullerton, E. E.; Liu, Z. Enhancing Spontaneous Emission Rates of Molecules Using Nanopatterned Multilayer Hyperbolic Metamaterials. *Nat. Nanotechnol.* **2014**, *9*, 48–53.

(23) Lin, H.-i.; Shen, K.-C.; Lin, S.-Y.; Haider, G.; Li, Y.-H.; Chang, S.-W.; Chen, Y.-F. Transient and Flexible Hyperbolic Metamaterials on Freeform Surfaces. *Sci. Rep.* **2018**, *8*, No. 9469.

(24) Lee, K. J.; Xiao, Y.; Woo, J. H.; Kim, E.; Kreher, D.; Attias, A.-J.; Mathevet, F.; Ribierre, J.-C.; Wu, J. W.; André, P. Charge-Transfer Dynamics and Nonlocal Dielectric Permittivity Tuned with Metamaterial Structures as Solvent Analogues. *Nat. Mater.* **2017**, *16*, 722–729.

(25) Lu, D.; Qian, H.; Wang, K.; Shen, H.; Wei, F.; Jiang, Y.; Fullerton, E. E.; Yu, P. K. L.; Liu, Z. Nanostructuring Multilayer Hyperbolic Metamaterials for Ultrafast and Bright Green Ingan Quantum Wells. *Adv. Mater.* **2018**, No. 1706411.

(26) Tielrooij, K.-J.; Hesp, N. C. H.; Principi, A.; Lundeberg, M. B.; Pogna, E. A. A.; Banszerus, L.; Mics, Z.; Massicotte, M.; Schmidt, P.; Davydovskaya, D.; Purdie, D. G.; Goykhman, I.; Soavi, G.; Lombardo, A.; Watanabe, K.; Taniguchi, T.; Bonn, M.; Turchinovich, D.; Stampfer, C.; Ferrari, A. C.; Cerullo, G.; Polini, M.; Koppens, F. H. L. Out-of-Plane Heat Transfer in Van Der Waals Stacks through Electron–Hyperbolic Phonon Coupling. *Nat. Nanotechnol.* **2018**, *13*, 41–46.

(27) Chandrasekar, R.; Wang, Z.; Meng, X.; Azzam, S. I.; Shalaginov, M. Y.; Lagutchev, A.; Kim, Y. L.; Wei, A.; Kildishev, A. V.; Boltasseva, A.; Shalae, V. M. Lasing Action with Gold Nanorod Hyperbolic Metamaterials. *ACS Photonics* **2017**, *4*, 674–680.

(28) Lin, H.-i.; Shen, K.-C.; Liao, Y.-M.; Li, Y.-H.; Perumal, P.; Haider, G.; Cheng, B. H.; Liao, W.-C.; Lin, S.-Y.; Lin, W.-J.; Lin, T.-Y.; Chen, Y.-F. Integration of Nanoscale Light Emitters and

Hyperbolic Metamaterials: An Efficient Platform for the Enhancement of Random Laser Action. *ACS Photonics* **2018**, *5*, 718–727.

(29) Shen, K. C.; Ku, C. T.; Hsieh, C.; Kuo, H. C.; Cheng, Y. J.; Tsai, D. P. Deep-Ultraviolet Hyperbolic Metacavity Laser. *Adv. Mater.* **2018**, *30*, No. 1706918.

(30) Haider, G.; Lin, H.-I.; Yadav, K.; Shen, K.-C.; Liao, Y.-M.; Hu, H.-W.; Roy, P. K.; Bera, K. P.; Lin, K.-H.; Lee, H.-M.; Chen, Y.-T.; Chen, F.-R.; Chen, Y.-F. A Highly-Efficient Single Segment White Random Laser. *ACS Nano* **2018**, *12*, 11847–11859.

(31) Shen, K.-C.; Hsieh, C.; Cheng, Y.-J.; Tsai, D. P. Giant Enhancement of Emission Efficiency and Light Directivity by Using Hyperbolic Metacavity on Deep-Ultraviolet Algan Emitter. *Nano Energy* **2018**, *45*, 353–358.

(32) Ferrari, L.; Smalley, J. S. T.; Fainman, Y.; Liu, Z. Hyperbolic Metamaterials for Dispersion-Assisted Directional Light Emission. *Nanoscale* **2017**, *9*, 9034–9048.

(33) Galfsky, T.; Sun, Z.; Considine, C. R.; Chou, C.-T.; Ko, W.-C.; Lee, Y.-H.; Narimanov, E. E.; Menon, V. M. Broadband Enhancement of Spontaneous Emission in Two-Dimensional Semiconductors Using Photonic Hypercrystals. *Nano Lett.* **2016**, *16*, 4940–4945.

(34) Sreekanth, K. V.; Krishna, K. H.; De Luca, A.; Strangi, G. Large Spontaneous Emission Rate Enhancement in Grating Coupled Hyperbolic Metamaterials. *Sci. Rep.* **2014**, *4*, No. 6340.

(35) Huang, G.; Mei, Y. Electromagnetic Wave Propagation in a Rolled-up Tubular Microcavity. *J. Mater. Chem. C* **2017**, *5*, 2758–2770.

(36) Lin, X.; Fang, Y.; Zhu, L.; Zhang, J.; Huang, G.; Wang, J.; Mei, Y. Self-Rolling of Oxide Nanomembranes and Resonance Coupling in Tubular Optical Microcavity. *Adv. Opt. Mater.* **2016**, *4*, 936–942.

(37) Cao, H.; Zhao, Y. G.; Ho, S. T.; Seelig, E. W.; Wang, Q. H.; Chang, R. P. H. Random Laser Action in Semiconductor Powder. *Phys. Rev. Lett.* **1999**, *82*, 2278–2281.

(38) Wiersma, D. S. The Physics and Applications of Random Lasers. *Nat. Phys.* **2008**, *4*, 359–367.

(39) Redding, B.; Choma, M. A.; Cao, H. Speckle-Free Laser Imaging Using Random Laser Illumination. *Nat. Photonics* **2012**, *6*, 355.

(40) Polson, R. C.; Vardeny, Z. V. Random Lasing in Human Tissues. *Appl. Phys. Lett.* **2004**, *85*, 1289–1291.

(41) Chang, S.-W.; Liao, W.-C.; Liao, Y.-M.; Lin, H.-I.; Lin, H.-Y.; Lin, W.-J.; Lin, S.-Y.; Perumal, P.; Haider, G.; Tai, C.-T.; Shen, K.-C.; Chang, C.-H.; Huang, Y.-F.; Lin, T.-Y.; Chen, Y.-F. A White Random Laser. *Sci. Rep.* **2018**, *8*, No. 2720.

(42) Sun, T.-M.; Wang, C.-S.; Liao, C.-S.; Lin, S.-Y.; Perumal, P.; Chiang, C.-W.; Chen, Y.-F. Stretchable Random Lasers with Tunable Coherent Loops. *ACS Nano* **2015**, *9*, 12436–12441.

(43) Liao, W.-C.; Liao, Y.-M.; Su, C.-T.; Perumal, P.; Lin, S.-Y.; Lin, W.-J.; Chang, C.-H.; Lin, H.-I.; Haider, G.; Chang, C.-Y.; Chang, S.-W.; Tsai, C.-Y.; Lu, T.-C.; Lin, T.-Y.; Chen, Y.-F. Plasmonic Carbon-Dot-Decorated Nanostructured Semiconductors for Efficient and Tunable Random Laser Action. *ACS Appl. Nano Mater.* **2018**, *1*, 152–159.

(44) Roy, P. K.; Haider, G.; Lin, H.-I.; Liao, Y.-M.; Lu, C.-H.; Chen, K.-H.; Chen, L.-C.; Shih, W.-H.; Liang, C.-T.; Chen, Y.-F. Multicolor Ultralow-Threshold Random Laser Assisted by Vertical-Graphene Network. *Adv. Opt. Mater.* **6** 1800382. DOI: 10.1002/adom.201800382.

(45) Shi, X.; Liao, Y.-M.; Lin, H.-Y.; Tsao, P.-W.; Wu, M.-J.; Lin, S.-Y.; Hu, H.-H.; Wang, Z.; Lin, T.-Y.; Lai, Y.-C.; Chen, Y.-F. Dissolvable and Recyclable Random Lasers. *ACS Nano* **2017**, *11*, 7600–7607.

(46) Liao, Y.-M.; Lai, Y.-C.; Perumal, P.; Liao, W.-C.; Chang, C.-Y.; Liao, C.-S.; Lin, S.-Y.; Chen, Y.-F. Highly Stretchable Label-Like Random Laser on Universal Substrates. *Adv. Mater. Technol.* **2016**, *1*, No. 1600068.

(47) Bohren, C. F.; Huffman, D. R. Absorption and Scattering by an Arbitrary Particle. *Absorption and Scattering of Light by Small Particles*, 2nd ed.; Wiley-VCH Verlag GmbH, 2007; pp 57–81.

(48) Ford, G. W.; Weber, W. H. Electromagnetic Interactions of Molecules with Metal Surfaces. *Phys. Rep.* **1984**, *113*, 195–287.

(49) Dowling, J. P. Spontaneous Emission in Cavities: How Much More Classical Can You Get? *Found. Phys.* **1993**, *23*, 895–905.

(50) Novotny, L.; Hecht, B. *Principles of Nano-Optics*; Cambridge Univ. Press: Cambridge, 2006.

(51) Gu, L.; Tumkur, T. U.; Zhu, G.; Noginov, M. A. Blue Shift of Spontaneous Emission in Hyperbolic Metamaterial. *Sci. Rep.* **2014**, *4*, No. 4969.

(52) Slobozhanyuk, A. P.; Ginzburg, P.; Powell, D. A.; Iorsh, I.; Shalin, A. S.; Segovia, P.; Krasavin, A. V.; Wurtz, G. A.; Podolskiy, V. A.; Belov, P. A.; Zayats, A. V. Purcell Effect in Hyperbolic Metamaterial Resonators. *Phys. Rev. B* **2015**, *92*, No. 195127.

(53) Sanchis, L.; Cryan, M. J.; Pozo, J.; Craddock, I. J.; Rarity, J. G. Ultrahigh Purcell Factor in Photonic Crystal Slab Microcavities. *Phys. Rev. B* **2007**, *76*, No. 045118.

(54) Badolato, A.; Hennessy, K.; Atatüre, M.; Dreiser, J.; Hu, E.; Petroff, P. M.; Imamoglu, A. Deterministic Coupling of Single Quantum Dots to Single Nanocavity Modes. *Science* **2005**, *308*, 1158–1161.

(55) Kristensen, P. T.; Hughes, S. Modes and Mode Volumes of Leaky Optical Cavities and Plasmonic Nanoresonators. *ACS Photonics* **2014**, *1*, 2–10.

(56) Xiao, Y.-F.; Li, B. B.; et al. High Quality Factor, Small Mode Volume, Ring-Type Plasmonic Microresonator on a Silver Chip. *J. Phys. B: At., Mol. Opt. Phys.* **2010**, *43*, No. 035402.

(57) Ginzburg, P.; Roth, D. J.; Nasir, M. E.; Segovia, P.; Krasavin, A. V.; Levitt, J.; Hirvonen, L. M.; Wells, B.; Suhling, K.; Richards, D.; Podolskiy, V. A.; Zayats, A. V. Spontaneous Emission in Non-Local Materials. *Light Sci. Appl.* **2017**, *6*, No. e16273.

(58) Liu, J.; Garcia, P. D.; Ek, S.; Gregersen, N.; Suhr, T.; Schubert, M.; Mork, J.; Stobbe, S.; Lodahl, P. Random Nanolasing in the Anderson Localized Regime. *Nat. Nanotechnol.* **2014**, *9*, 285–289.

(59) Sapienza, L.; Thyrestrup, H.; Stobbe, S.; Garcia, P. D.; Smolka, S.; Lodahl, P. Cavity Quantum Electrodynamics with Anderson-Localized Modes. *Science* **2010**, *327*, 1352–1355.

(60) Luan, F.; Gu, B.; Gomes, A. S. L.; Yong, K.-T.; Wen, S.; Prasad, P. N. Lasing in Nanocomposite Random Media. *Nano Today* **2015**, *10*, 168–192.

(61) Rao, K. S.; El-Hami, K.; Kodaki, T.; Matsushige, K.; Makino, K. A Novel Method for Synthesis of Silica Nanoparticles. *J. Colloid Interface Sci.* **2005**, *289*, 125–131.

(62) Enustun, B. V.; Turkevich, J. Coagulation of Colloidal Gold. *J. Am. Chem. Soc.* **1963**, *85*, 3317–3328.

(63) Kim, J. Y.; Yoon, S. B.; Yu, J.-S. Fabrication of Nanocapsules with Au Particles Trapped inside Carbon and Silica Nanoporous Shells. *Chem. Commun.* **2003**, *6*, 790–791.

# **Nanoscale Core-Shell Hyperbolic Structures for Ultralow Threshold Laser Action: An Efficient Platform for the Enhancement of Optical Manipulation**

Hung-I Lin<sup>1,2†</sup>, Kanchan Yadav<sup>3,4†</sup>, Kun-Ching Shen<sup>5</sup>, Golam Haider<sup>2</sup>, Pradip Kumar Roy<sup>2</sup>, Monika Kataria<sup>2</sup>, Ting-Jia Chang<sup>2</sup>, Yao-Hsuan Li<sup>1</sup>, Tai-Yuan Lin<sup>6</sup>, Yit-Tsong Chen<sup>3</sup>, and Yang-Fang Chen<sup>1,2,7\*</sup>

<sup>1</sup> Graduate Institute of Applied Physics, National Taiwan University, Taipei 106, Taiwan

<sup>2</sup> Department of Physics, National Taiwan University, Taipei 106, Taiwan

<sup>3</sup> Department of Chemistry, National Taiwan University, Taipei 106, Taiwan

<sup>4</sup> Nanoscience and Nanotechnology Program, Taiwan International Graduate Program, Institute of Physics, Academia Sinica, Taipei 115, Taiwan

<sup>5</sup> Research Center for Applied Sciences, Academia Sinica, Taipei 115, Taiwan

<sup>6</sup> Institute of Optoelectronic Sciences, National Taiwan Ocean University, Keelung 202, Taiwan

<sup>7</sup> Advanced Research Center for Green Materials Science and Technology, National Taiwan University, Taipei 106, Taiwan

† The authors contribute equally.

\*corresponding author: Yang-Fang Chen: [yfchen@phys.ntu.edu.tw](mailto:yfchen@phys.ntu.edu.tw)

**1. Transmission electron microscopy (TEM) image of the nanoscale core-shell hyperbolic structure.**

From the TEM image (Figure S1) we can observe a silica NP as core (16 nm diameter of silica core in the center, represented by the white dotted circle) surrounded by the shell (consisting of 1st layer of 5 nm Au NP followed by 3 nm of 2nd silica coating layer, which is represented by the red dotted circle, Note: The 1st layer Au NP covers the whole silica core and also some Au NPs are embedded in the silica shell). Then, the second layer of Au NPs (represented by the small yellow dotted circles) forms a thin layer of Au shell (represented by the blue dotted circles).

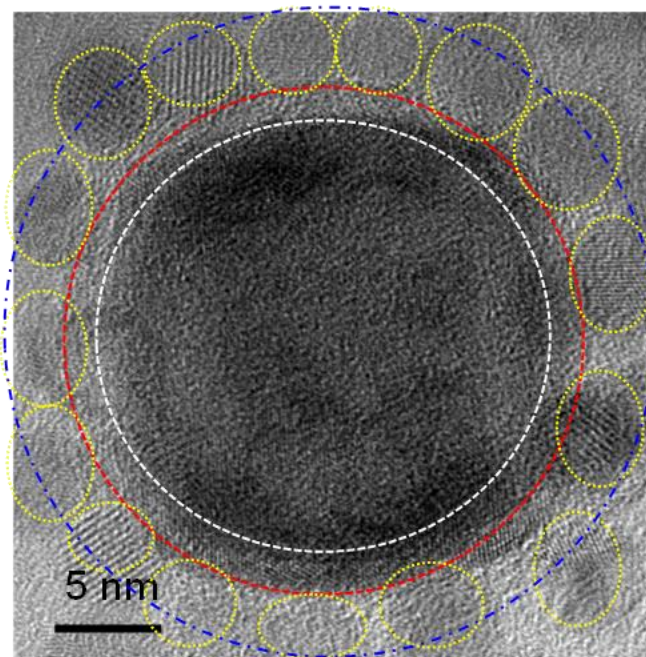


**Figure S1** | TEM image of the nanoscale core-shell hyperbolic structure.

## 2. Zeta potential tells the surface charge of the moieties.

In the reaction, the silica coated NP has been functionalized using mercaptopropyl triethoxy silane (MPTMS) to form SH@Silica NPs. Since, MPTMS contain thiol group (SH) which contributes to negative charge (as observed in the zeta measurement, *i.e.* -19.1 mV) as shown in Fig. S2. Later, Au NP functionalization with MPTMS to form Au@Silica NPs shifted the zeta value to a more negative value (*i.e.* -29.2 mV). Again, after the next MPTMS conjugation for the second layer (*i.e.* SH@Silica-Au@Silica NPs), the zeta value shifted back to a less negative value (*i.e.* -19.8 mV). And, followed by the second layer of Au NP conjugation (Au@Silica-Au@Silica), the zeta potential gets back to a more negative value (*i.e.* -30.0 mV).

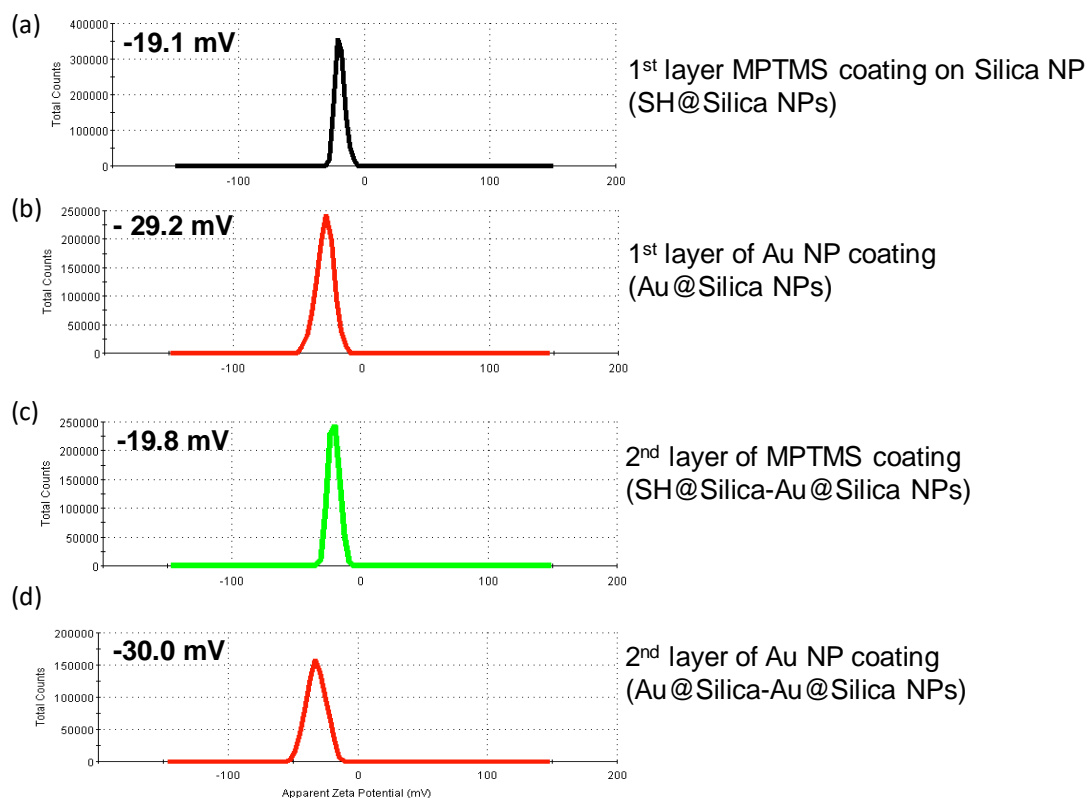


**Figure S2 | Zeta potential shows the surface charge of the moieties** (a) 1<sup>st</sup> layer MPTMS coating on Silica NP (SH@Silica NPs). (b) 1<sup>st</sup> layer of Au NP coating (Au@Silica NPs). (c) 2<sup>nd</sup> layer of MPTMS coating (SH@Silica-Au@Silica NPs). (d) 2<sup>nd</sup> layer of Au NP coating (Au@Silica-Au@Silica NPs).

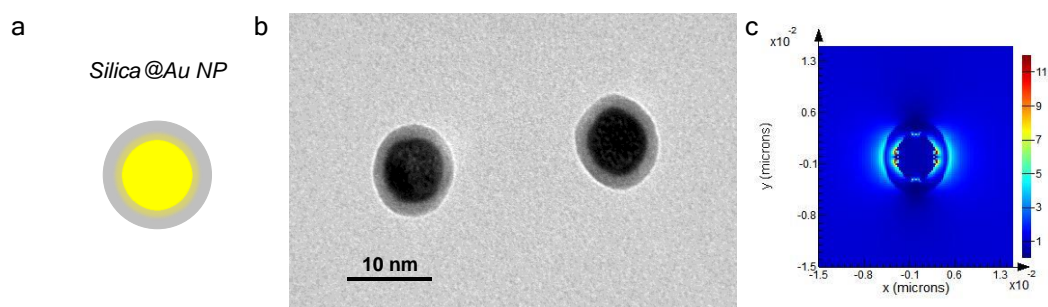
### 3. Schematic diagram of SiO<sub>2</sub> (Silica)@gold (Au) nanoparticle (NP) as a reference.

Figure S3a depicts the Silica@Au NP as a standard plasmonic-based reference sample.

The radius of Au NP is 3 nm with covering another 2 nm thick of Silica. The diameter

is 10 nm. Figure S3b is its TEM image. Figure S3c is the distribution of  $|E|^2$  around the

Silica@Au NP.



**Figure S3** | (a) Schematic diagram of Silica@Au NP as a reference sample. (b) The corresponding TEM image. (c) The distributions of  $|E|^2$  around the Silica@Au NP.

#### 4. The effective permittivity of the nanoscale core-shell hyperbolic structure.

In a very recently publication,<sup>1</sup> Wang *et al.* also used two pairs of SiO<sub>2</sub>/Au multishell nanostructures, defined as metaparticles, and then displayed a hyperbolic dispersion. To prove the used of characteristic of hyperbolic dispersion, they calculated the effective permittivity of the metal-dielectric multishells. We calculate the effective permittivity of the metal-dielectric multishells with the thickness of SiO<sub>2</sub> (3 nm)/Au (5 nm) as shown in Fig. S4. With the negative component of effective permittivity ( $\epsilon_{\theta}$ ) above the wavelength regions of 450 nm, the metal-dielectric multishells can be deemed as the hyperbolic dispersion.

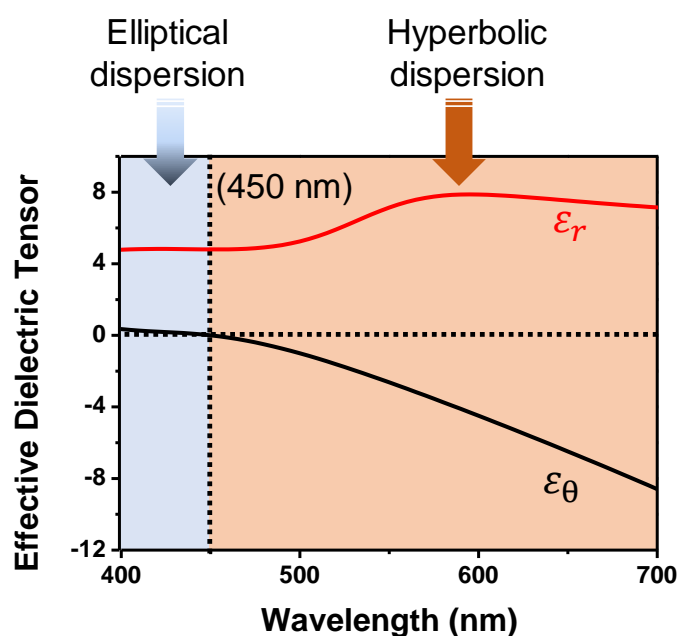


**Figure S4 | The effective permittivity of the nanoscale core-shell hyperbolic structure.** Light blue and light red regions are the wavelength regions of elliptical and hyperbolic dispersion, respectively. Black dashed lines are the transition wavelength from elliptical dispersion to hyperbolic dispersion. The transition wavelength for the nanoscale core-shell hyperbolic structure is 450 nm.

## 5. Lifetime dynamics of the nanoscale core-shell hyperbolic structure.

Figures S5(a), S5(b), S5(c) and S5(d) present the lifetime measurements of the nanoscale core-shell hyperbolic structure mixed with 4-(dicyanomethylene)-2-tert-butyl-6-(1,1,7,7-tetramethyljulolidin-4-yl-vinyl)-4H-pyran (DCJTB) dye molecules in a volume ratio of 4:1, 3:1, 1:1 and 1:2, respectively. All the emission spectra were excited by a 374 nm pulsed diode laser.

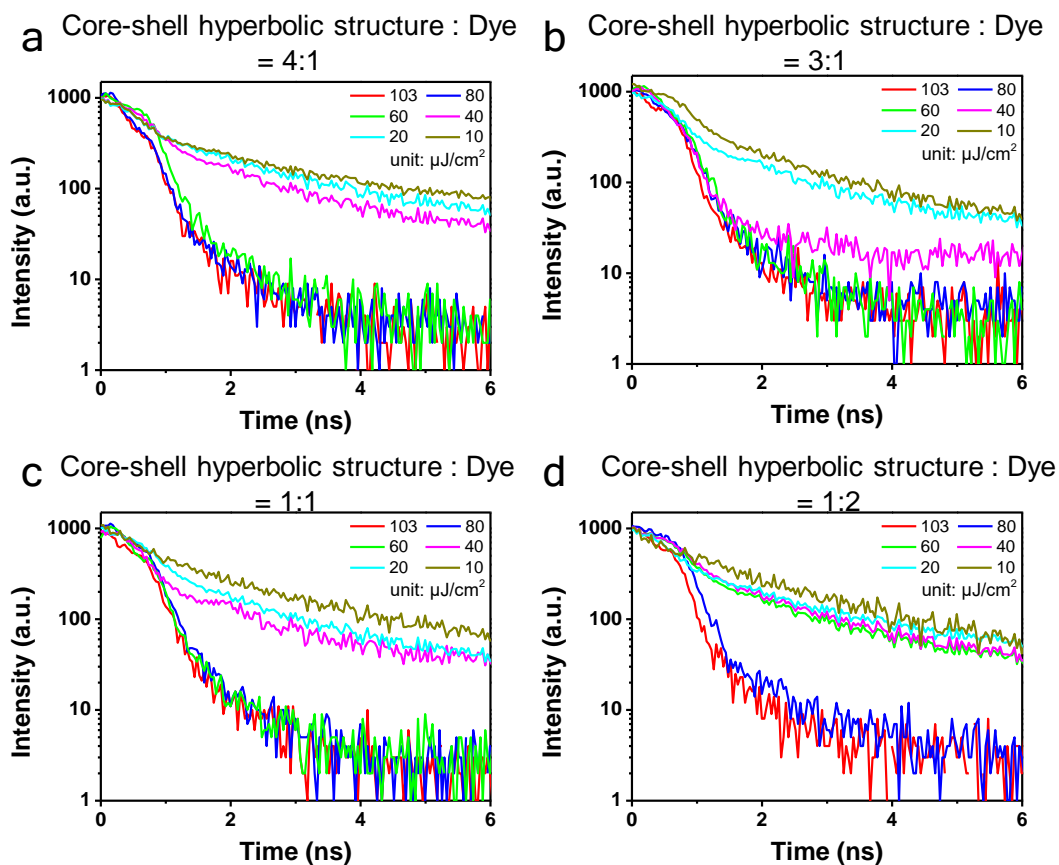


**Figure S5** | (a), (b), (c) and (d) The lifetime measurements of the nanoscale core-shell hyperbolic structure mixed with DCJTB dye molecules in a volume ratio of 4:1, 3:1, 1:1 and 1:2, respectively.

## **6. Spontaneous emission-fluorescence emission from DCJTB dye molecules mixed with Silica@Au NPs.**

Figure S6(a) presents the top-view scanning electron microscope (SEM) image of the Silica@Au NPs mixed with DCJTB dye molecules in a volume ratio of 4:1. Figure S6(b) is the corresponding emission spectra. Figures S6(c), S6(e), S6(g) and S6(i) are the SEM images in a volume ratio of 3:1, 2:1, 1:1 and 1:2, respectively. Figures S6(d), S6(f), S6(h) and S6(j) are the corresponding emission spectra. The emission spectra were excited by a 374 nm pulsed diode laser. Note that all the Silica@Au NP samples only demonstrate spontaneous emission without any lasing peaks.

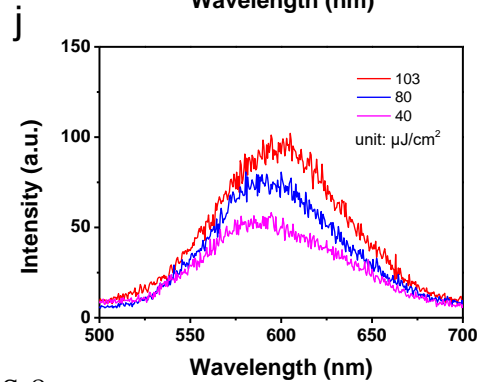
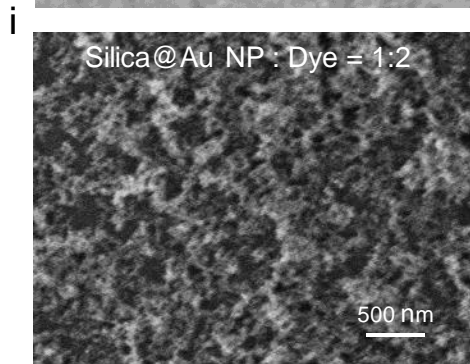
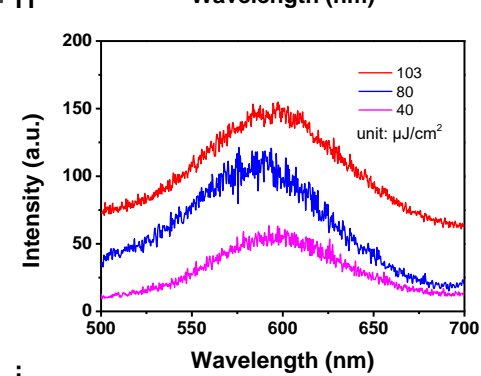
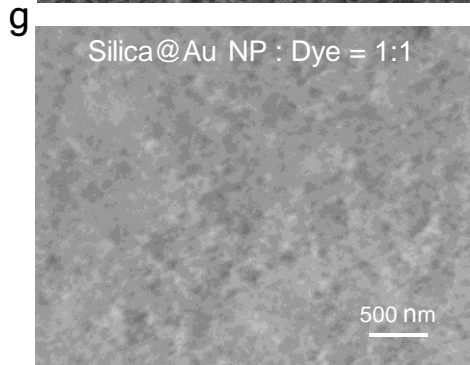
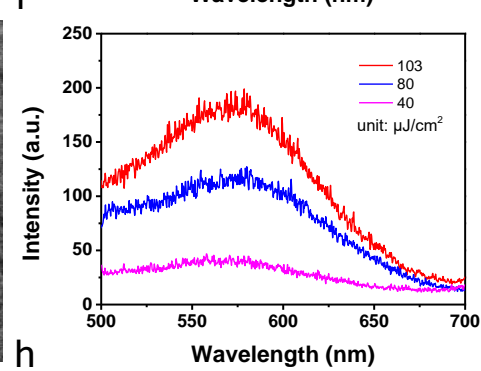
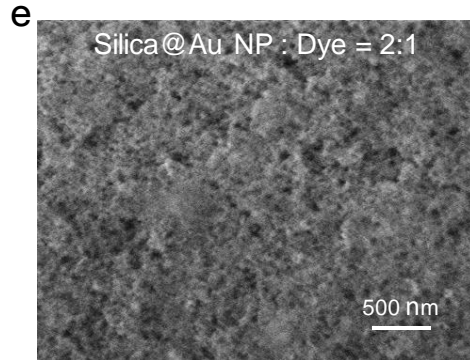
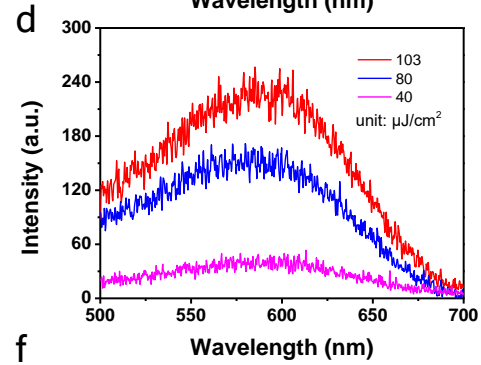
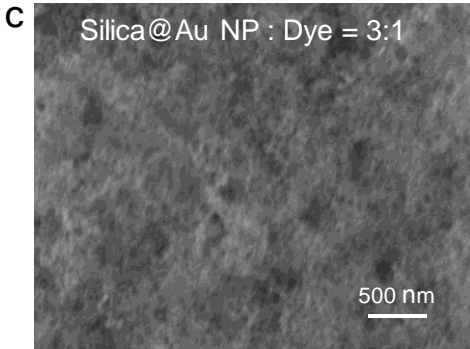
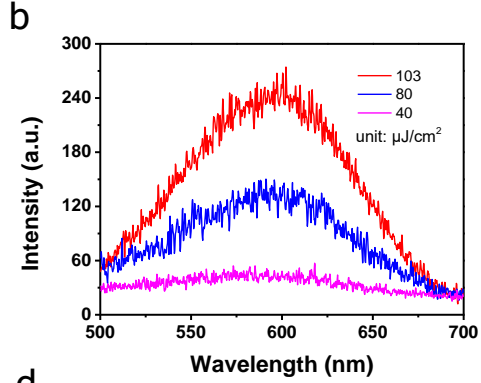
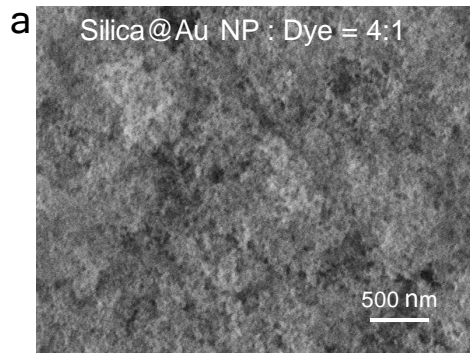


**Figure S6 | Spontaneous emission based on Silica@Au NPs.** (a) The top-view SEM image of Silica@Au NPs mixed with DCJTB dye molecules in a volume ratio of 4:1. (b) The corresponding emission spectra. All the emission spectra were excited by a 374 nm pulsed diode laser. (c), (e), (g) and (i) The SEM images in a volume ratio of 3:1, 2:1, 1:1 and 1:2, respectively. (d), (f), (h) and (j) The corresponding emission spectra.

## 7. Spontaneous emission-fluorescence emission from DCJTB dye molecule.

Figures S7(a), S7(b) and S7(c) show the peak emission intensity, FWHM and lifetime measurements as a function of pumping energy density.

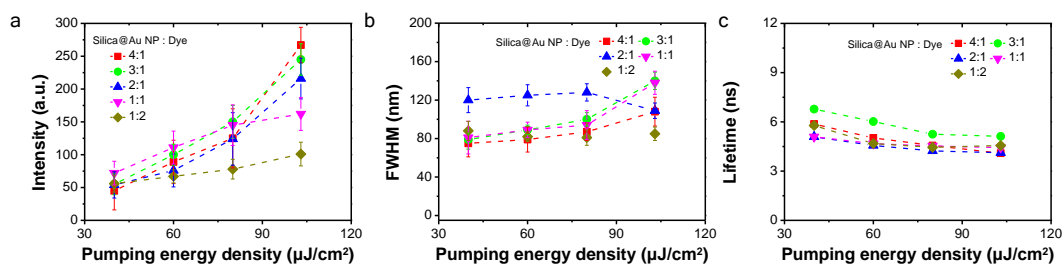


**Figure S7 | Characterization of spontaneous emission.** (a) The peak emission intensity. (b) The FWHM. (c) The lifetime as a function of pumping energy density.

## 8. Spontaneous emission-fluorescence emission from DCJTB dye molecule.

Figure S8a show the top-view SEM image of the DCJTB dye molecule. The morphology shows relative flat, which is not suitable for the formation of closed-loop path due to multiple scattering to achieve the random laser action. Figure S8b is the photoluminescence spectra for the DCJTB dye molecules. Figure S8c is the corresponding emission intensity and FWHM. The sample only demonstrates spontaneous emission instead of lasing peaks. Figure S8d is the lifetime measurement.

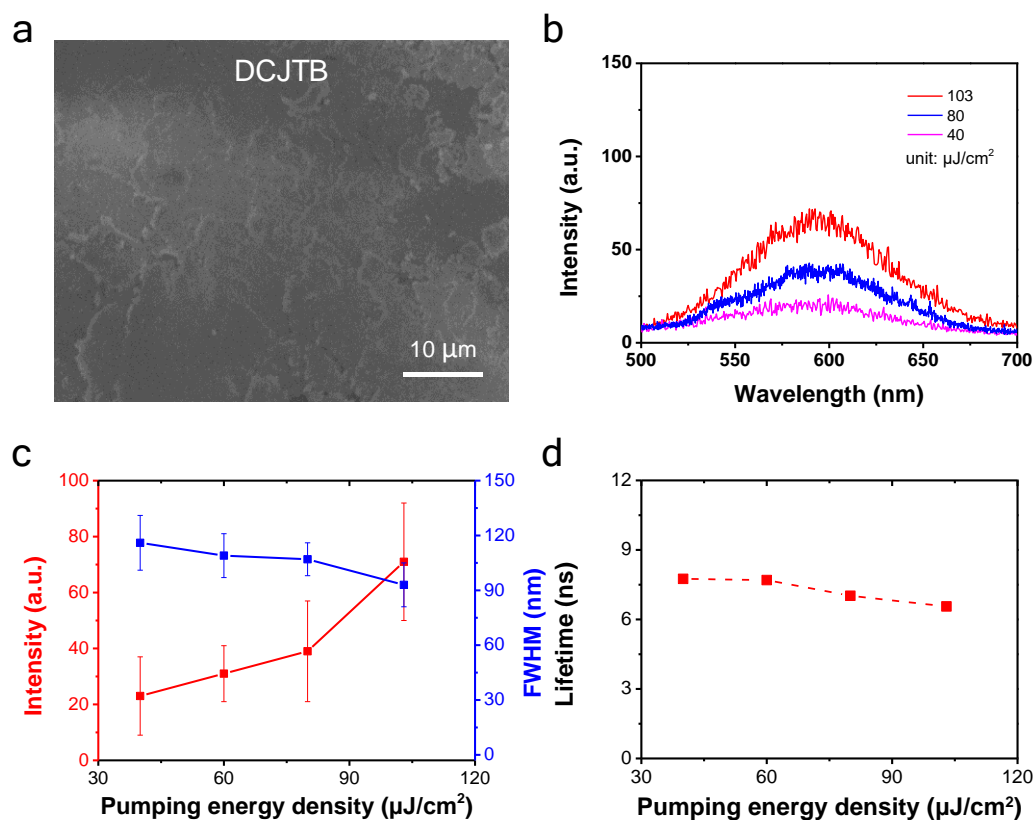


**Figure S8** | (a) is the top-view SEM image of the DCJTB dye molecule. (b) The photoluminescence measurements for the DCJTB dye molecule using 374 nm pulsed diode laser, respectively. (c) is the corresponding emission photoluminescence intensity and FWHM with error bars within one standard deviation of the mean. (d) The lifetime measurement.

## 9. Distributions of electric field intensity ( $|E|^2$ ).

Figure S9 shows the distributions of  $|E|^2$  and the corresponding three-dimensional (3D) components for the nanoscale core-shell hyperbolic structure and Silica@Au NP. The central emission wavelength is set at 590 nm.

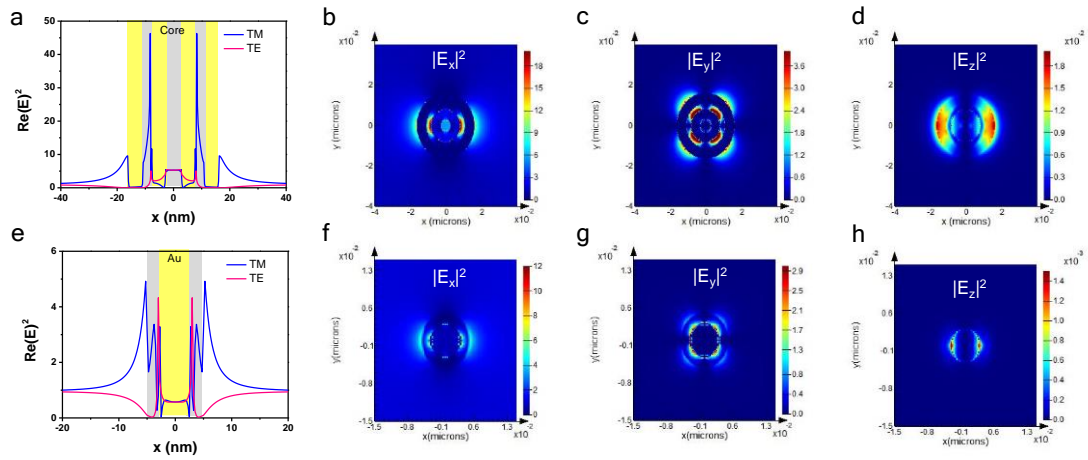


**Figure S9** | To realize the localized surface plasmon resonance (LSPR) effect, the cross-sectional  $|E|^2$  distributions of transverse magnetic (TM) and transverse electric (TE) modes for (a) the nanoscale core-shell hyperbolic structure. (b-d) are the corresponding 3D components of  $|E_x|^2$ ,  $|E_y|^2$  and  $|E_z|^2$ , respectively. (e) The cross-sectional  $|E|^2$  distributions of TM and TE modes for Silica@Au NP. (f-h) are the corresponding 3D components of  $|E_x|^2$ ,  $|E_y|^2$  and  $|E_z|^2$ , respectively. All the simulation results are performed under a normally incident light at a wavelength of 590 nm.

## 10. Radiation pattern.

Figure S10 presents the radiation patterns for the nanoscale core-shell hyperbolic structure (Fig. S10a) and Silica@Au NP (Fig. S10b) of the scattered electric field along  $XY$ ,  $XZ$  and  $YZ$  planes, demonstrating these two structures with a radial symmetry in 3D spaces.

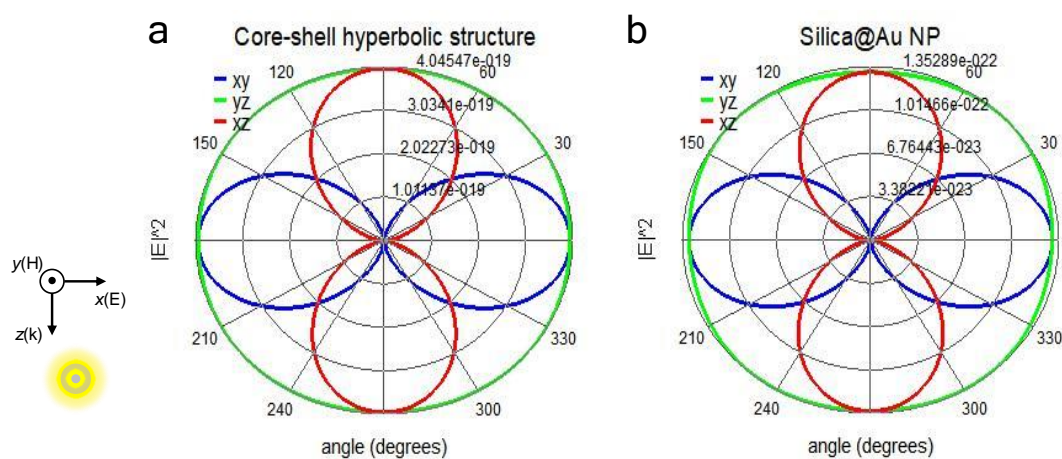


**Figure S10 | Radiation patterns.** (a) and (b) are the radiation patterns of the scattered electric field along  $XY$ ,  $XZ$  and  $YZ$  planes for the nanoscale core-shell hyperbolic structure and Silica@Au NP, respectively. Inset image is the normally incident light at the wavelength of 580 nm.

## 11. Simulation method of scattering efficiency.

We further discuss the scattering efficiency based on the Mie theory. It is defined by the scattering cross-section ( $\sigma_{scat}$ ) divided by the scattering cross-sectional area that is a projected plane perpendicular to the incident light ( $A_{scat}$ ). Both of the  $A_{scat}$  for nanoscale core-shell hyperbolic structure and Silica@Au NP is  $\pi R^2$ , where  $R$  is the radius of 35 nm. The scattering cross-section is determined by:<sup>2</sup>

$$\sigma_{scat} = \frac{2\pi}{k^2} \sum_{n=1}^{\infty} (2n+1) (|a_n|^2 + |b_n|^2), \quad (S1)$$

where  $k$  is the wave number,  $a_n$  and  $b_n$  are the scattering coefficients:

$$a_n = \frac{m\psi_n(mx)\psi_n'(x) - \psi_n(x)\psi_n'(mx)}{m\psi_n(mx)\xi_n'(x) - \xi_n(x)\psi_n'(mx)}, \quad (S2)$$

$$b_n = \frac{\psi_n(mx)\psi_n'(x) - m\psi_n(x)\psi_n'(mx)}{\psi_n(mx)\xi_n'(x) - m\xi_n(x)\psi_n'(mx)}, \quad (S3)$$

where  $\psi_n$  and  $\xi_n$  are determined from Riccati-Bessel functions.  $x$  is the size parameter and  $m$  is the relative refractive index:

$$x = kR = \frac{2\pi NR}{\lambda}, \quad (S4)$$

$$m = \frac{k_1}{k} = \frac{N_1}{N}, \quad (S5)$$

where  $N_1$  and  $N$  are the refractive indices of nanoparticles and the surrounding medium, respectively.

## 12. Scattering cross-section at different incident angles.

Figure S11 shows the scattering cross-section at different incident angle ( $\theta$ ) sweeping from normal ( $\theta = 0^\circ$ ) to  $\theta = 50^\circ$  in a wavelength region of 500-700 nm.

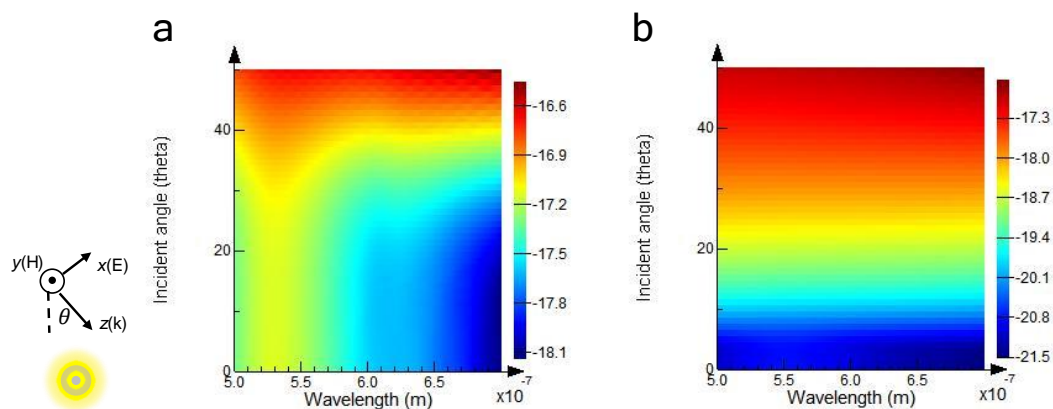


**Figure S11 | Scattering cross-section at different incident angles.** (a) and (b) are the scattering cross-section for the nanoscale core-shell hyperbolic structure and Silica@Au NP, respectively. Inset image is the incident light with a tilt angle ( $\theta$ ). We simulated from normal ( $\theta = 0^\circ$ ) to  $\theta = 50^\circ$  with a wavelength region of 500-700 nm. All the figures are plotted in a logarithmic scale.

### 13. Purcell factor within 50 nm away from the surface of NP.

Figure S12 shows the Purcell factors within 50 nm away from the surface of NP with a dipole emitter source. To stress the significance of the near-field coupling enhancement, we plotted the Purcell factors in logarithmic scales.

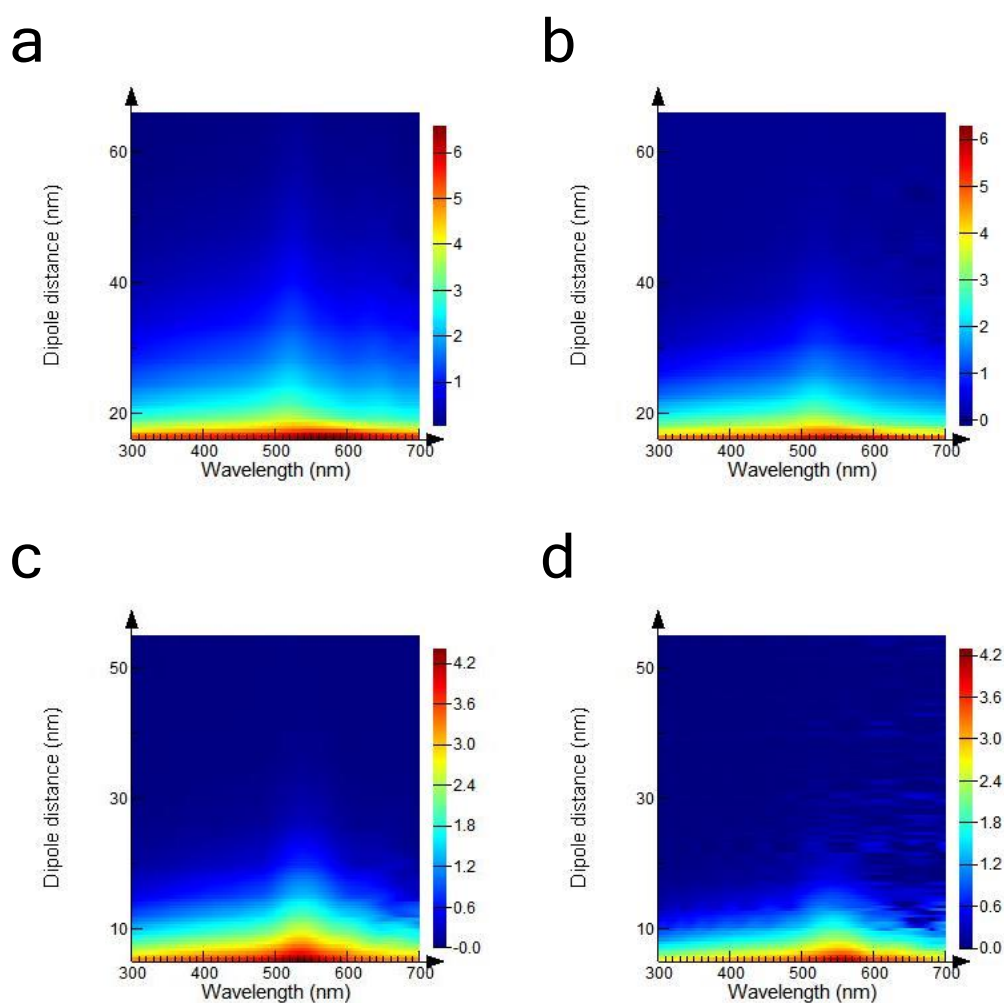


**Figure S12 | Theoretical calculation of Purcell factors.** (a) and (b) are the Purcell factors within 50 nm with a dipole emitter perpendicular and parallel to the nanoscale core-shell hyperbolic structure, respectively. (c) and (d) are the Purcell factors within 50 nm with a dipole emitter perpendicular and parallel to the Silica@Au NP, respectively. All the figures are plotted in logarithmic scales.

#### **14. Theoretical analysis with different refractive indices.**

We compare the refractive index of Au adapted from Pelik *et. al.*,<sup>3</sup> and Johnson and Christy *et. al.*,<sup>4</sup> which has been commonly used in previous literatures for bulk materials as well as the refractive index of Au from Lemarchand<sup>5</sup> for the nanoscale materials. The simulated scattering efficiency, Purcell factor, local density of states ( $\rho_p$ ) and spontaneous decay rate ( $\gamma$ ) are shown in Figure S13. The observed trends are similar with less discrepancy between the actual refractive index for nanoscale materials and the literature values for bulk materials. Indeed, Wang *et al.*'s<sup>1</sup> simulation results also used the refractive index of Au from Johnson and Christy *et. al.*,<sup>4</sup> showing the reasonable and matched resonance peaks and intensities as compared with their experimentally measured extinction spectra and simulated optical cross section.

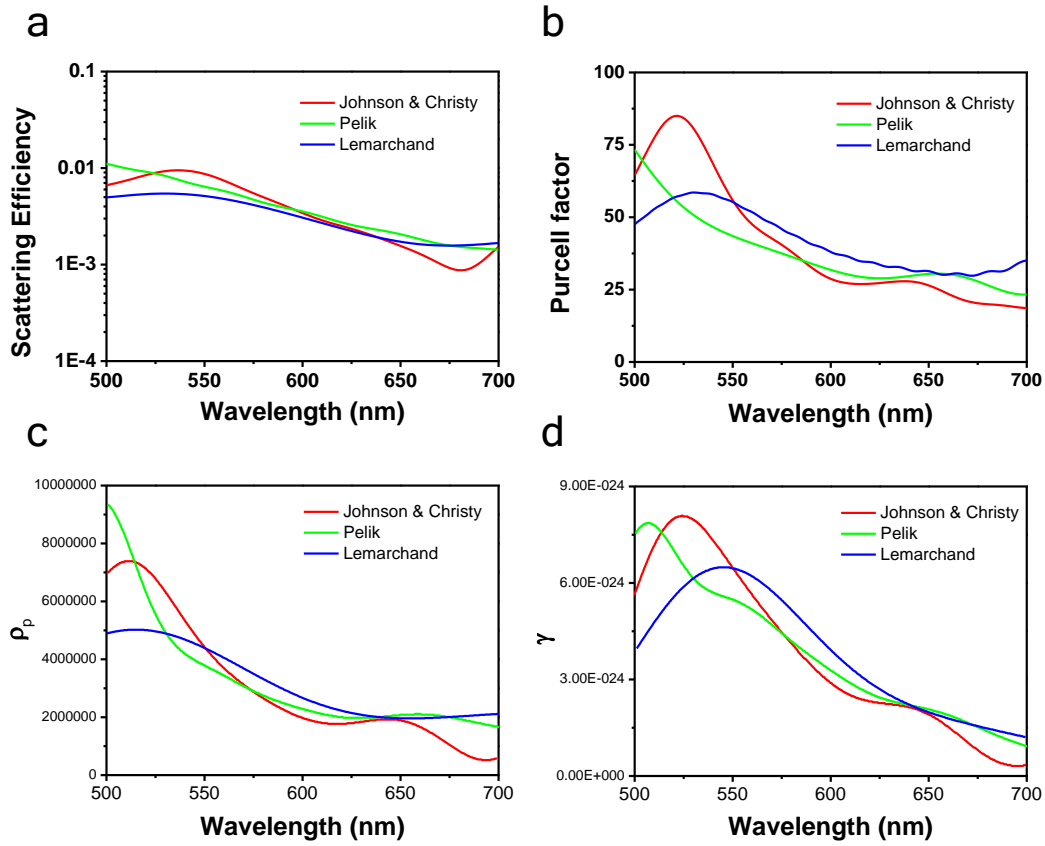


**Figure S13 | Theoretical analysis with different refractive indices.** The refractive index of Au was adapted from Pelik *et. al.*,<sup>2</sup> and Johnson and Christy *et. al.*,<sup>3</sup> which has been commonly used in previous literatures for bulk materials. In this study, we also used the refractive index of Au from Lemarchand<sup>4</sup> for the nanoscale materials. (a) and (b) are the scattering efficiency and the Purcell factor with dipole sources above the surface for 10 nm, respectively. (c) and (d) are the local density of states ( $\rho_p$ ) and the spontaneous decay rate ( $\gamma$ ), respectively. All the simulation spectra are set at wavelength region of 500-700 nm.

## 15. Optical characterizations of the cross-sectional profiles.

Figure S14a shows the energy distributions of the cross-sectional profiles for the nanoscale core-shell hyperbolic structure and Fig. S14b is the Silica@Au NP.

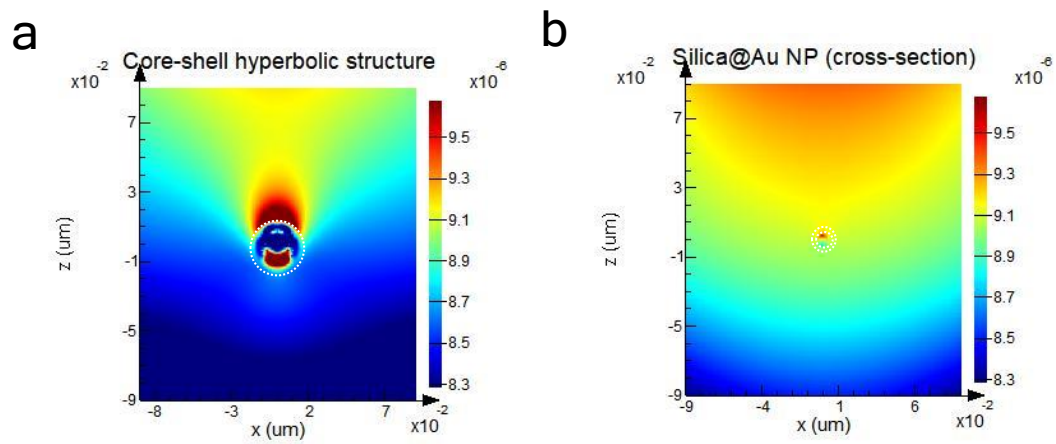


**Figure S14 | Optical characterizations of the cross-sectional profiles.** (a) The energy distributions of the cross-sectional profiles for the nanoscale core-shell hyperbolic structure and (b) Silica@Au NP.

## 16. Optical properties for the same thickness of Au/Silica as multilayer thin film structure.

Here, we simulated the same thickness of 2 pairs Au/Silica multilayer thin film structure as another comparison to emphasize the importance of the nanoscale core-shell hyperbolic structure. Figure S15a shows the time decay of field envelope components. Figures S15b and S15c are the energy distributions to analysis the mode volume ( $36553200 \text{ nm}^3$ ) for top-view and cross-sectional profiles, respectively.

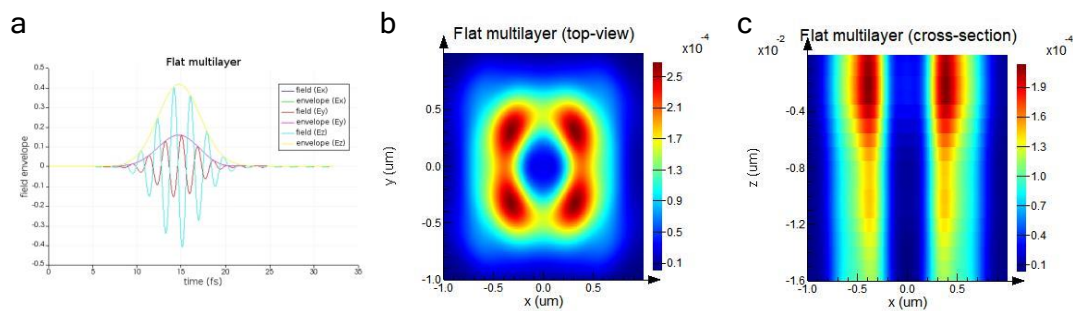


**Figure S15 | Optical properties of 2 pairs Au/Silica multilayer thin film structure.**

(a) the time decay of field envelope components. (b) and (c) are the energy distributions to analysis the mode volume for top-view and cross-sectional profiles, respectively.

### 17. Simulation of scattering efficiency for multi-pairs of nanoscale core-shell hyperbolic structure.

Certainly, it is anticipated that with increasing the number of multishells (*e.g.*, 2, 3 and 4 pairs), the scattering efficiency can increase dramatically as shown in Fig. S16. In our work, we further demonstrated the nanoscale core-shell hyperbolic structure not only can enhance the local field, but also enables to achieve the stimulated emission with an ultralow lasing threshold ( $\sim 30 \mu\text{J}/\text{cm}^2$ ). Therefore, both of the novel metaparticles as studied by Wang *et al.* and the nanoscale core-shell hyperbolic structure designed by us can lead promising functionalities of plasmonic-based applications.

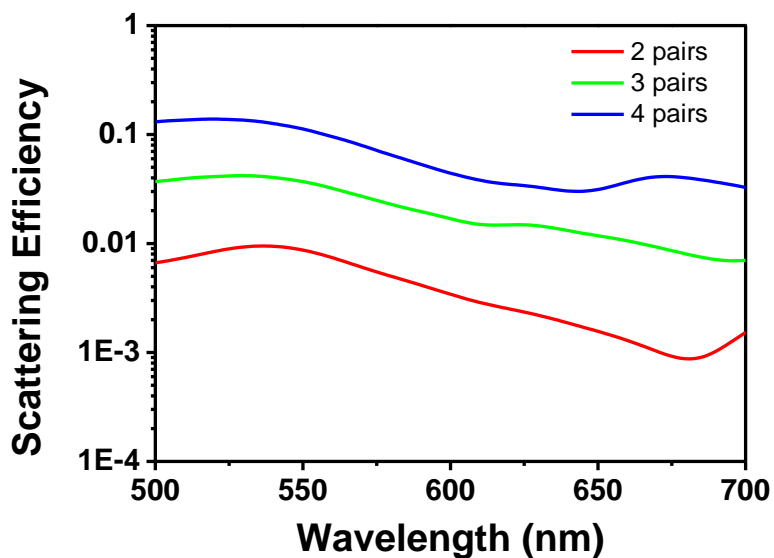
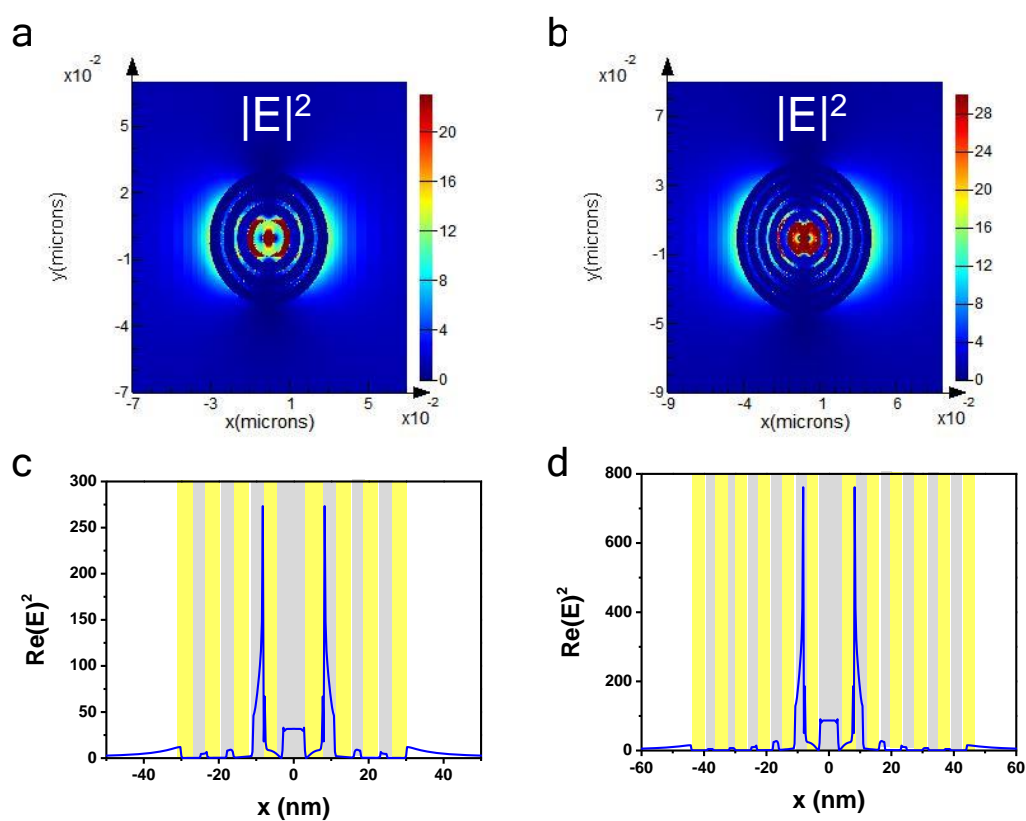


Figure S16 | Scattering efficiency of the nanoscale core-shell hyperbolic structure with multi-pairs (*e.g.*, 2, 3 and 4 pairs) in a logarithmic scale.

## 18. Simulation of $|E|^2$ distributions for multi-pairs of nanoscale core-shell hyperbolic structure.

Figure S17 shows the simulation results of  $|E|^2$  distributions and the transverse magnetic (TM) mode profiles for multi-pairs of the nanoscale core-shell hyperbolic structure. The central emission wavelength remains at 590 nm under normal direction of incident light. With accumulating the pairs of shell component for nanoscale core-shell hyperbolic structure, each increasing layer for Silica (Au) is fixed at 3 (5) nm. For example, with considering the 4 (6) pairs of nanoscale core-shell hyperbolic structure, the radius is 30 (44) nm.



**Figure S17** | (a) and (b) are the distributions of  $|E|^2$  around the 4 and 6 pairs of nanoscale core-shell hyperbolic structure, respectively. (c) and (d) are the corresponding TM mode profiles. All the results are simulated under normal incident of light at a wavelength of 590 nm.

## 19. Simulation of spontaneous emission dynamics for multi-pairs of nanoscale core-shell hyperbolic structure.

The simulations of Purcell factors, local density of states (LDOS) and spontaneous decay rate for multi-pairs (*e.g.*, 4 and 6 pairs) of the nanoscale core-shell hyperbolic structure are shown in Fig. S18. The dipole source is placed 10 nm above the outermost surface to determine Purcell factors. We simulated the wavelength region of 500-700 nm.

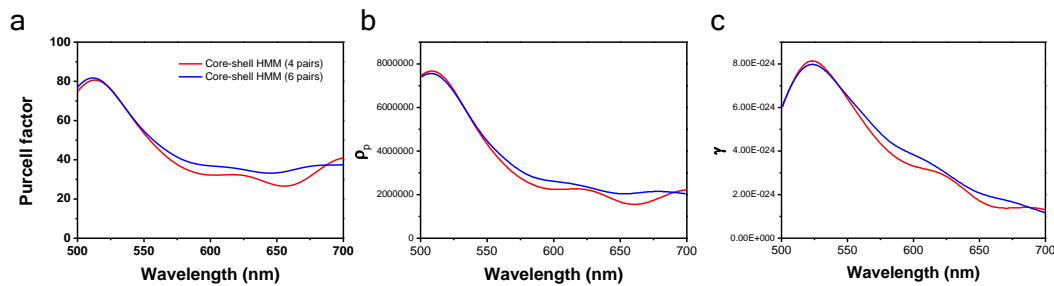


**Figure S18** | (a) The Purcell factors with a dipole source around the outermost surface for 10 nm for multi-pairs of nanoscale core-shell hyperbolic structure. (b) The LDOS. (c) The spontaneous decay rate.

## 20. Purcell factor of the core-carrying emitter at the center core.

Figure S19 shows the pronounced Purcell factor at the center of the nanoscale core-shell hyperbolic structure as a platform for core-carrying emitter.

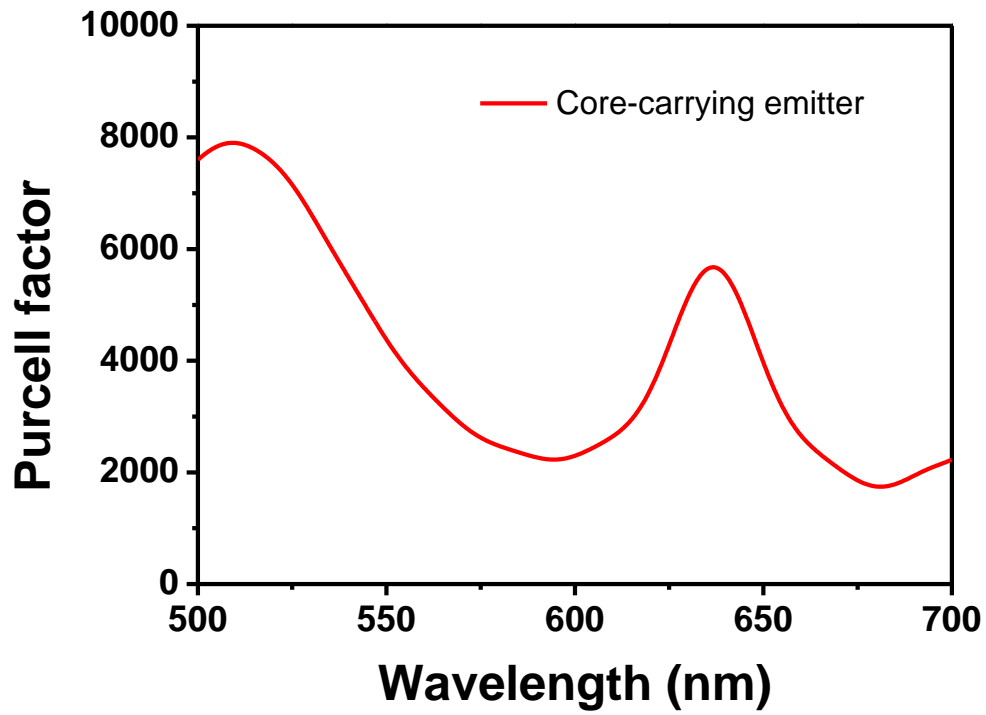


**Figure S19** | The Purcell factor at the center of the nanoscale core-shell hyperbolic structure.

## References

1. Wang, P.; Krasavin, A. V.; Viscomi, F. N.; Adawi, A. M.; Bouillard, J.-S. G.; Zhang, L.; Roth, D. J.; Tong, L.; Zayats, A. V. Metaparticles: Dressing Nano-Objects with a Hyperbolic Coating. *Laser Photonics Rev.* **2018**, 1800179.
2. Bohren, C. F.; Huffman, D. R., Absorption and Scattering by an Arbitrary Particle. In *Absorption and Scattering of Light by Small Particles*, 2 ed.; Wiley-VCH Verlag GmbH: 2007; pp 57-81.
3. Palik, E. D. *Handbook of optical constants of solids*. Vol. 1, Ch. 3, 290-291 (Academic: San Diego, CA, 1997).
4. Johnson, P. B.; Christy, R. W. Optical Constants of the Noble Metals. *Phys. Rev. B* **1972**, 6, (12), 4370-4379.
5. Gao, L.; Lemarchand, F.; Lequime, M. Comparison of Different Dispersion Models for Single Layer Optical Thin Film Index Determination. *Thin Solid Films* **2011**, 520, (1), 501-509.